J. Fluid Mech. (2006), *vol.* 563, *pp.* 357–388.
doi:10.1017/S0022112006001340 Printed in the United Kingdom

Continuous mode transition and the effects of pressure gradient

By TAMER A. ZAKI[1] AND PAUL A. DURBIN[2]

[1]Mechanical Engineering, Imperial College, London, SW7 2AZ, UK
[2]Aerospace Engineering, Iowa State University, Ames, IA 50011, USA

(Received 28 March 2005 and in revised form 26 February 2006)

Continuous mode transition is an instance of the bypass route to boundary-layer turbulence. The stages that precede breakdown are explained in terms of continuous Orr–Sommerfeld and Squire spectra. In that context, the role of pressure gradient is less evident than it is in natural transition. Its role is investigated using linear theory and numerical simulations. Both approaches demonstrate that adverse pressure gradients enhance the coupling of low-frequency vortical disturbances to the boundary-layer shear. The result is stronger boundary-layer perturbation jets – or Klebanoff distortions. The correlation between the intensity of the perturbation jets and transition location is tested by direct numerical simulations of pairwise continuous mode interactions; such interactions can reproduce the entire transition process. The results confirm that stronger perturbation jets are more unstable, and hence provoke early transition in adverse pressure gradient. This is also consistent with the experimental observation that transition becomes independent of pressure gradient at high turbulent intensities. Under such conditions, boundary-layer streaks are highly unstable and transition is achieved swiftly, independent of the mean gradient in pressure.

1. Introduction

In what is called the orderly route to transition, Tollmien–Schlichting instability waves develop and break down (Kleiser & Zang 1991). The growth rate of Tollmien–Schlichting waves is very sensitive to pressure gradient. In zero and favourable pressure gradients (ZPG and FPG), Tollmien–Schlichting waves are subject to a weak viscous instability. In adverse pressure gradient (APG), the mean velocity profile has an inflection point and inviscid instability takes over, with viscosity becoming stabilizing. Consequently the growth rate increases greatly.

The alternative to the orderly route is called bypass transition (Morkovin 1969). By definition, bypass transition is not caused by Tollmien–Schlichting waves. Any role that pressure gradient plays in bypass transition cannot be attributed to inflectional mean flow profiles. The perspective that bypass is the complement to orderly transition suggests that it be studied by starting from the complement to Tollmien–Schlichting waves. The latter are the discrete modes of the Orr–Sommerfeld operator; their complement in Orr–Sommerfeld (O-S) theory is the continuous spectrum. Hence, in this paper we discuss pressure gradients from the perspective of continuous mode transition (Durbin & Zaki 2005). Our objective is to identify how pressure gradient can play a role within that context.

The continuous Orr–Sommerfeld modes are vortical eigen-solutions of the linear perturbation operator. They are oscillatory in the free stream, and damp with distance

into the boundary layer. Different modes penetrate the boundary layer to different depths. Therefore, a study of mode shape is key to understanding the interaction of free-stream vortical disturbances and the boundary-layer shear.

Grosch & Salwen (1978) provided plots of the continuous Orr–Sommerfeld mode shapes. However, their numerical method was inadequate for solving the eigenvalue problem in the frequency limit $\omega \sim O(1)$. Jacobs & Durbin (1998) proposed an alternative algorithm that enables accurate computation of the continuous modes at all frequencies. They also emphasized the importance of mode shape and of penetration depth. Maslowe & Spiteri (2001) applied a similar approach and discussed the effect of pressure gradient on mode shapes for the continuous spectrum of the Orr–Sommerfeld operator. Maslowe & Spiteri (2001) focused on the effect that pressure gradients have on the oscillation of the magnitude of the eigenfunction about a normalized value in the free stream. They predicted an increase in the amplitude of oscillation of Orr–Sommerfeld modes at the edge of the boundary layer for both adverse and favourable pressure gradients.

In the present paper, the interest is shifted to the effect of mean pressure gradient on modal penetration into the boundary layer. Penetrating three-dimensional Orr–Sommerfeld modes tilt the boundary-layer mean shear and, as a result, generate normal vorticity perturbations. This interaction is governed by the Squire equation for normal vorticity disturbance. Mathematically, the Orr–Sommerfeld forcing term in the Squire equation is the linearized tilting term in the three-dimensional vorticity equation. In the low-frequency limit, these perturbations give rise to the high-intensity elongated boundary-layer streaks. These streaks are jets in the perturbation field, in the sense that they are streamwise elongated strips of predominantly u velocity perturbation (Jacobs & Durbin 2000). The root mean squares of the instantaneous perturbation jets are known as Klebanoff 'modes' (these are not modes in the mathematical sense: Wu & Choudhari (2003) suggest the term Klebanoff distortions).

In bypass transition, the amplification of the low-frequency streaks is followed by the inception of turbulent spots and, finally, breakdown. In addition to causing early transition onset, adverse pressure gradient shortens the length of the transitional region of the flow. Higher spot inception and spreading rates in retarded flows are observed and well documented experimentally (Abu-Ghannam & Shaw 1980; Gostelow, Blunden & Walker 1994). In order to study spot spreading, Bowles & Smith (1995) solved the initial-value problem of an inviscid multi-scale disturbance in an otherwise laminar flow. The model problem of a piecewise-linear mean flow captures the correct spreading angle for spots in zero-pressure-gradient boundary layers. The same approach was extended by Brown & Smith (2002) in order to include the effect of pressure gradient. Their solution captures the wider spread angle of disturbances in adverse pressure gradient.

Abu-Ghannam & Shaw (1980) provide a good summary of the experimental findings regarding transition onset. Their figure 6 shows the dependence of transition location on pressure gradient, at various levels of free-stream turbulence intensity, T_u. In orderly transition, or the limit of zero turbulence intensity, the influence of APG on transition location is pronounced. This is due to the inviscid instability of the mean velocity profile, as well as the enhanced amplification of discrete mode triads in decelerated flows (Goldstein & Lee 1992; Corke & Gruber 1996). The influence of pressure gradient diminishes with increasing T_u. In the limit of high free-stream turbulence, $T_u > 3\,\%$, transition location is much farther upstream and, when expressed in terms of the momentum thickness Reynolds number R_θ, becomes independent of the pressure gradient. Even under moderate free-stream turbulence intensities, the

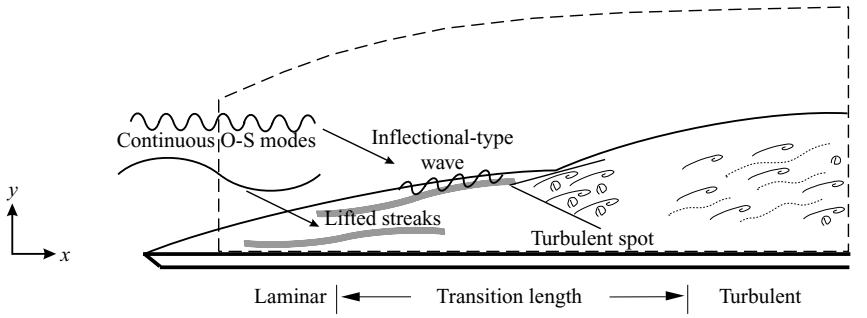

FIGURE 1. Schematic of continuous mode transition.

natural route to transition is completely *bypassed* (Hodson & Howell 2005). Therefore, the influence of pressure gradient in the bypass regime is not due to the inflectional mean velocity profile. Instead, the notion of *coupling* of the free-stream vortical disturbances to the boundary-layer shear, and the intensity of the streaks generated owing to that interaction, become important.

A coupling coefficient, Θ, was proposed by Zaki & Durbin (2005) in order to quantify the propensity of Orr–Sommerfeld continuous modes in the free stream to generate boundary-layer streaks. The definition of Θ is motivated by a resonance between Orr–Sommerfeld forcing and Squire mode response. The coupling coefficient is evaluated in the present paper for eigenfunctions of Falkner–Skan profiles. The results are suggestive of the effect of pressure gradient on streak intensity and, consequently, transition onset.

Linear theory is the starting point for our direct numerical simulations (DNS). A single low-frequency continuous Orr–Sommerfeld mode is prescribed at the inflow, and its spatial evolution computed in adverse, zero and favourable pressure gradients. The intensity of the boundary-layer streaks is examined for the various levels of mean pressure gradient. The trends observed in the DNS are also compared to those predicted by linear theory.

Direct numerical simulations go beyond linear theory to provide a fuller picture of transition. Jacobs & Durbin (2000) carried out DNS of bypass transition of a zero-pressure-gradient boundary layer forced by a fully turbulent free stream. In their simulations, it is seen that the low-frequency backward perturbation jets lift towards the edge of the boundary layer. There, they are exposed to the high-frequency non-penetrating disturbances in the free stream. This local interaction is destabilizing, and initiates breakdown of the laminar jet, leading to the appearance of a turbulent spot.

In an effort to isolate the essential interaction that leads to breakdown, Zaki & Durbin (2005) investigated continuous mode transition in zero pressure gradient (figure 1). Their computer simulations showed that the entire transition process is realizable through the interaction of only two Orr–Sommerfeld continuous mode eigenfunctions: one low-frequency, strong coupling disturbance, and one high-frequency mode. The former penetrates the boundary layer and induces the forward and backward perturbation jets. The latter high-frequency disturbance is filtered by the shear, and hence exists solely in the free stream. This mode interacts with the lifted backward jets only near the top of the boundary layer, causing an *inflectional* type of instability (which should not be confused with the inflection point of the mean velocity profile in orderly transition). The instability intensifies downstream, leading to breakdown into a turbulent spot.

Similar DNSs of pairwise mode interactions are performed herein. First, in the absence of pressure gradient, the simulations examine the dependence of transition location on the amplitude of the low-frequency inflow disturbance or, equivalently, the intensity of the boundary-layer streaks. The results verify whether higher-intensity backward perturbation jets are more susceptible to instability once they are exposed to high-frequency forcing at the upper edge of the boundary layer. This *bypass* mechanism, which commences at the top of the boundary layer, is therefore quite distinct from the near-wall inflection-point instability characteristic of natural transition. The ZPG results are followed by DNS of continuous mode transition in the presence of mean pressure gradient.

The next four sections of this paper address the influence of pressure gradient on the early stages of bypass transition in the context of linear perturbation theory. Section 2 includes the formulation of the linear perturbation problem. Section 3 discusses the effect of pressure gradient on the shape of the continuous Orr–Sommerfeld and Squire modes. In § 4, the solution to the initial-value problem of normal-vorticity generation due to Orr–Sommerfeld forcing is evaluated. Both the universality of the shape of Klebanoff distortions and the influence of pressure gradients on the amplitude of boundary-layer streaks are highlighted. Whether the coupling coefficient, Θ, captures the dependence of the intensity of boundary-layer streaks on flow acceleration is addressed in § 5. Linear theory is followed by a discussion of our direct numerical simulations of single and pairwise continuous Orr–Sommerfeld mode interaction in § 6. A summary of the results is presented in the last section.

2. Linear theory: the Orr–Sommerfeld/Squire eigenvalue problem

Linear theory provides a starting point for studying the process of boundary-layer instability and transition. The linear evolution of a small disturbance about a viscous parallel mean flow $U(y)$ is described by the Orr–Sommerfeld and Squire equations. The pair corresponds to the normal velocity, v, and vorticity, η, equations (Drazin & Reid 1995),

$$\partial_t \begin{bmatrix} v \\ \eta \end{bmatrix} = \begin{bmatrix} \Delta^{-1}\{d_y^2 U \partial_x + (R^{-1}\Delta - U\partial_x)\Delta\} & 0 \\ -d_y U \partial_z & R^{-1}\Delta - U\partial_x \end{bmatrix} \begin{bmatrix} v \\ \eta \end{bmatrix}, \tag{2.1}$$

where Δ is the Laplacian operator, and Δ^{-1} is its formal inverse. The boundary layer 99 % thickness, δ, and the free-stream velocity, U_∞, are the characteristic length and velocity scales. The Reynolds number is therefore defined as $R = U_\infty \delta/\nu$.

The Orr–Sommmerfeld/Squire eigenvalue problem can be derived by invoking Fourier representation in the homogeneous spatial directions and in time:

$$\begin{bmatrix} v(\boldsymbol{x}, t) \\ \eta(\boldsymbol{x}, t) \end{bmatrix} = \begin{bmatrix} \phi(y)\exp(-\mathrm{i}\omega_{os} t) \\ \chi(y)\exp(-\mathrm{i}\omega_{sq} t) \end{bmatrix} \exp(\mathrm{i}(k_x x + k_z z)).$$

Here, we consider the *homogeneous* Squire operator, and therefore the eigenvalue problems for normal velocity and vorticity become independent, and are

$$-\begin{bmatrix} \mathrm{i}\omega_{os}\phi \\ \mathrm{i}\omega_{sq}\chi \end{bmatrix} = \begin{bmatrix} \mathscr{L} & 0 \\ 0 & \mathscr{S} \end{bmatrix} \begin{bmatrix} \phi \\ \chi \end{bmatrix}, \tag{2.2}$$

where

$$\mathscr{L} = \Delta^{-1}\{\mathrm{i}k_x U'' + [\Delta(\Delta)/R] - \mathrm{i}k_x U\Delta\},$$
$$\mathscr{S} = [(\Delta/R) - \mathrm{i}k_x U].$$

In semi-bounded flows, $y \geqslant 0$, the Orr–Sommerfeld and Squire eigenvalue problems possess a discrete spectrum, with eigenvalues ω_n, $n = 1, 2, 3, \ldots, N$, and a continuous spectrum ω_{k_y}. The discrete eigenfunctions satisfy $\lim_{y\to\infty} \phi_n, \chi_n(y) = 0$; the continuous eigenfunctions satisfy $\lim_{y\to\infty} \phi_{k_y}, \chi_{k_y}(y)$ are bounded. The latter are oscillatory in the free stream and provide an expansion basis for disturbances (Grosch & Salwen 1978).

Note that the coupling term, $\mathscr{C} = \mathrm{i}k_z U'$, from equation (2.1), does not appear in the eigenvalue problem (2.2), and therefore does not cause non-normality of the eigenfunctions. Instead, this term is considered to force the homogeneous Squire operator,

$$(R^{-1}\Delta - U\partial_x)\eta - \partial_t \eta = \mathscr{C}\phi \exp(\mathrm{i}(k_x x + k_z z - \omega_{os} t)). \tag{2.3}$$

The forcing can be resonant with the normal vorticity operator. In the case of the discrete Tollmien–Schlichting and Squire modes, direct resonance does not take place because the discrete eigenvalues of the two operators do not coincide. Only a 'near-resonant' behaviour is possible when the discrete eigenvalues of the two operators become sufficiently similar (Benney & Gustavsson 1981). In the case of the continuous spectrum, *exact*, or direct, resonance takes place between the continuous Orr–Sommerfeld modal forcing and the Squire response. This resonance is a simple consequence of them having exactly the same dispersion relation and, hence, the same continuous eigenvalues (Zaki & Durbin 2005). The solution to the initial-value problem, therefore, exhibits linear growth in time prior to its viscous decay.

3. Mode shape

Continuous Orr–Sommerfeld and Squire modes are oscillatory in the free stream, and evanescent inside the boundary layer. Their mode shape provides a natural basis for expanding a general free-stream vortical disturbance into its 'Fourier' components. The influence of each eigenfunction on the boundary layer can then be evaluated independently. A study of mode shape, therefore, explains the process by which particular frequency components of the free-stream disturbance penetrate the boundary layer.

The extent to which the Orr–Sommerfeld and Squire continuous eigenfunctions penetrate the boundary layer is dependent on the wall-normal wavenumber k_y, frequency ω, Reynolds number R, and the mean shear distribution (Jacobs & Durbin 1998). This dependence is captured in the eigensolution for a piecewise-linear mean flow profile,

$$\begin{aligned} U(y) &= U_\infty, \qquad\quad y > 0, \\ U(y) &= U_\infty + \tau y, \quad y < 0. \end{aligned}$$

The shape of the eigenfunction in the region of shear, $y < 0$, is given by an Airy function

$$\psi(y) = c_1 \,\mathrm{Ai}\left[(\mathrm{i}\omega R\tau)^{1/3}\left(y + \frac{\mathrm{i}k_y^2}{R\omega\tau}\right)\right]. \tag{3.1}$$

For small distances into the shear region, $|y| < k_y^2/R\omega\tau$, the eigenfunction is oscillatory. However, for larger values of $|y|$, the solution decays exponentially. Therefore, the quantity $k_y^2/R\omega\tau$ determines the extent of penetration of the eigenfunction into the boundary layer.

Pressure gradients do not alter the dependence of penetration depth on R, ω or k_y. The effect of increasing R or ω remains enhanced sheltering, while higher k_y enhances penetration. These trends are demonstrated in figures 2 to 4, where the continuous Orr–Sommerfeld modes are computed numerically. The mean flow is a Falkner–Skan

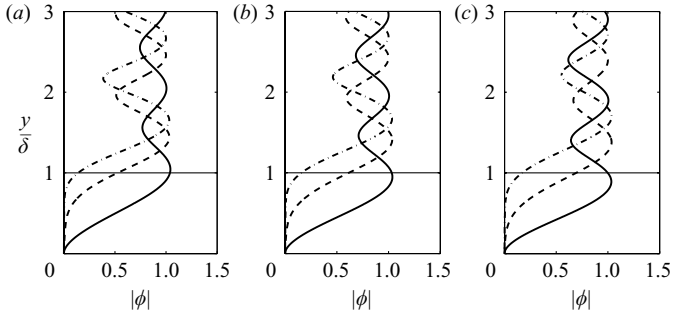

FIGURE 2. Effect of R on penetration depth ($\omega = \pi, k_z = \pi, k_y = \pi$), ——, $R = 10$; - - -, $R = 100$; — · —, $R = 1000$. (*a*) $\beta = -0.18$, (*b*) $\beta = 0$, (*c*) $\beta = +0.5$.

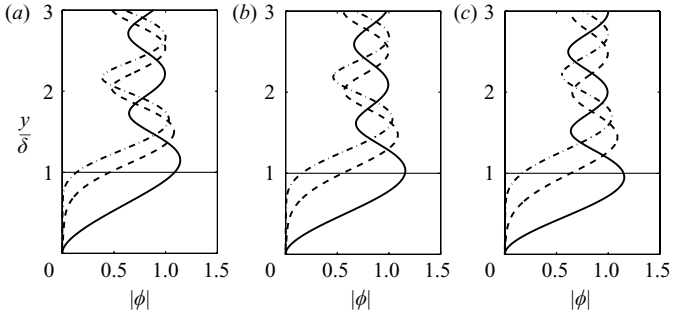

FIGURE 3. Effect of ω on penetration depth ($R = 1000, k_z = \pi, k_y = \pi$), ——, $\omega = \pi/100$; - - -, $\omega = \pi/10$; — · —, $\omega = \pi$. (*a*) $\beta = -0.18$, (*b*) $\beta = 0$, (*c*) $\beta = +0.5$.

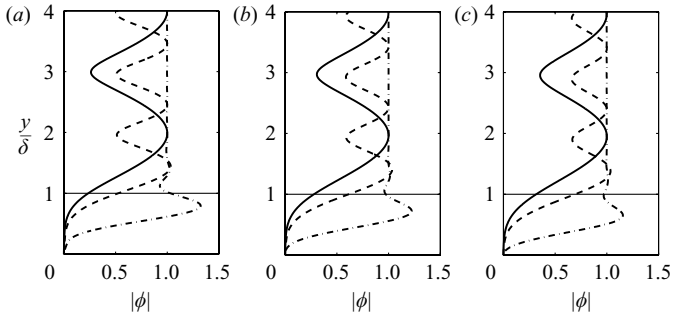

FIGURE 4. Effect of k_y on penetration depth ($R = 100, \omega = \pi, k_z = \pi$), ——, $k_y = \pi/2$; - - -, $k_y = \pi$; — · —, $k_y = 4\pi$. (*a*) $\beta = -0.18$, (*b*) $\beta = 0$, (*c*) $\beta = +0.5$.

similarity solution for the accelerating free stream, $U_\infty(x) = Kx^{\beta/(2-\beta)}$. The dependence of penetration depth on R, ω and k_y is similar in retarded and accelerated flows, as demonstrated in the figures.

Pressure gradients cause a variation in the mean shear distribution, τ, and as a result alter the sheltering ability of the boundary layer. It is therefore expected that the shape of continuous modes and the extent of their penetration into the boundary layer are affected. Figure 5 shows the mean velocity profile for three pressure gradient parameters. In APG, the shear is higher close to the edge of the boundary layer than in FPG. As a result, it is expected that in APG the Orr–Sommerfeld modes

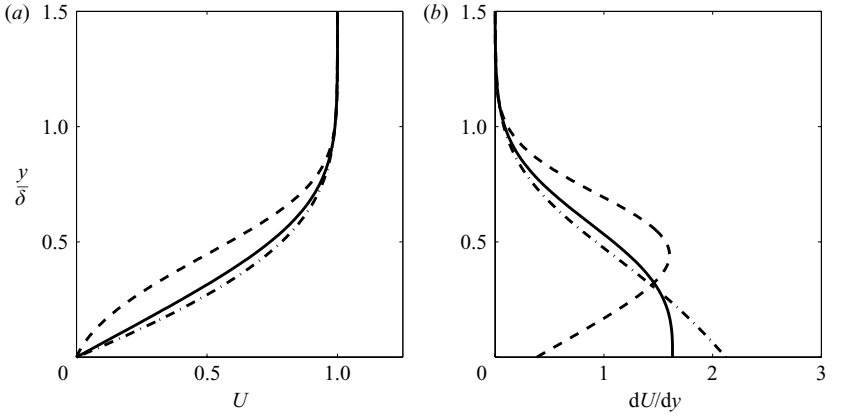

FIGURE 5. Mean velocity profiles for different pressure gradient parameters. - - -, $\beta = -0.19$; ——, $\beta = 0$; — · —, $\beta = +0.2$.

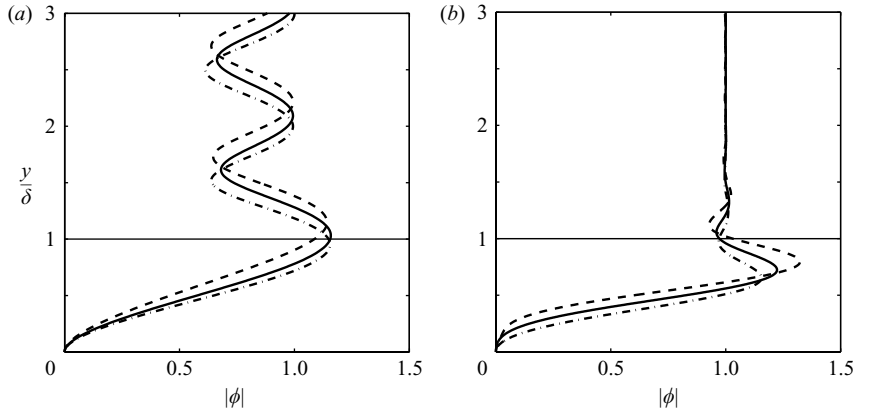

FIGURE 6. Effect of pressure gradient parameter on penetration depth. - - -, $\beta = -0.19$; ——, $\beta = 0$; — · —, $\beta = +0.5$ (*a*) $R = 1000$, $\omega = \pi/100$, $k_y = \pi$, $k_z = \pi$, (*b*) $R = 100$, $\omega = \pi$, $k_y = 4\pi$, $k_z = \pi$.

penetrate less than in zero and favourable pressure gradients. This assertion is verified in figure 6, although the effect is not large. In that figure, the Orr–Sommerfeld modes in favourable pressure gradient are the most penetrating, while least penetrating in adverse pressure gradient.

In figure 6, the amplitude of the Orr–Sommerfeld eigenfunction was normalized to unity in the free stream. Figure 6(*a*) shows that both the adverse and favourable pressure-gradient modes have increased amplitude of oscillation in the free stream, consistent with the results of Maslowe & Spiteri (2001). However, at the edge of the boundary layer, both have a smaller magnitude than the zero-pressure-gradient case. Figure 6(*b*) shows the amplitude of the APG mode is highest, followed by ZPG, and finally FPG at the edge of the boundary layer. The variation in amplitude is therefore wavenumber and Reynolds-number dependent. A clear, general statement cannot be made regarding the effect of pressure gradient on the oscillation in the magnitude of the eigenfunctions.

However, the variation of sheltering or penetration depth with pressure gradient is consistent. Adverse pressure gradient enhances shear sheltering and, as a result,

reduces penetration. Conversely, accelerated flows exhibit reduced sheltering – that is, enhanced penetration of continuous modes. This dependence is shown in figure 6: the Orr–Sommerfeld modes penetrate to lower y/δ in FPG than in zero and adverse pressure gradient.

It is important to note that the pressure gradient parameters considered here are large. Nevertheless, their effect on penetration is limited (see figure 6). It can therefore be concluded that the variation in sheltering due to pressure gradient is not a substantial effect. If this effect were significant, transition in retarded flows, where sheltering is enhanced, would be delayed. Instead, it is generally accepted that retarded flows experience earlier transition, while accelerated flows are more stable (Abu-Ghannam & Shaw 1980).

Therefore, the experimentally established effect of pressure gradients on transition onset is at odds with the variation in shear sheltering. In order to account for the discrepancy, attention is shifted to the notion of coupling: the propensity of penetrating Orr–Sommerfeld modes to force the normal vorticity equation, and generate boundary-layer streaks. Enhanced coupling in retarded flows would offset the minor improvement in sheltering, and explain early transition in adverse pressure gradients. Similarly, weak coupling in accelerated flows would offset the mild enhancement in penetration depth, and explain delayed transition in favourable pressure gradients. In the next section, in order to investigate coupling, we turn to the initial-value problem (IVP) of Squire response to Orr–Sommerfeld forcing.

Shifting the focus to coupling does not undermine the importance of the concept of shear sheltering. This physical mechanism is perhaps the only one capable of explaining the variation of mode shape within the boundary layer, and hence addressing the question of boundary-layer receptivity to modal components of a general free-stream vortical disturbance. Also, the boundary-layer response to forcing by a single Orr–Sommerfeld mode is a packet of Squire modes with different k_y (see next section, and Zaki & Durbin 2005). The superposition of the Squire spectrum cancels in the free stream, but not in the boundary layer, owing to the dependence of penetration on wall-normal wavenumber. The incomplete cancellation gives rise to the well known Klebanoff distortions.

A study of continuous spectrum mode shape is therefore relevant. However, it is not sufficient to explain the experimentally observed trends in transition location under flow acceleration. For this, we next consider the initial-value problem, and the notion of coupling.

4. The initial-value problem

Penetrating three-dimensional, continuous Orr–Sommerfeld modes force the Squire operator resonantly. The response, a superposition of Squire eigenfunctions, gives rise to boundary-layer streaks (Zaki & Durbin 2005). The maximum intensity of the streaks, reaching magnitudes of the order of 10 % of U_∞, has been documented in the experimental and numerical literature (Kendall 1991; Westin *et al.* 1994; Jacobs & Durbin 2000). These elongated streamwise perturbations can be understood as normal vorticity response to tilting of the mean vorticity by the forcing term $\mathrm{i}k_z U'\phi(y)$ in equation (2.3). Two factors are therefore important in determining the intensity of the streaks: the penetration depth of the Orr–Sommerfeld mode $\phi(y)$, and the distribution of the mean shear U'. The former was addressed in the section on mode shape. Here, we consider fully penetrating Orr–Sommerfeld modes. It remains for us to discuss the variation in mean shear with pressure gradient, and the implications on the Squire response to Orr–Sommerfeld forcing.

In adverse pressure gradient, the shear distribution is in favour of generating strong boundary-layer jets. The location of the maximum shear is away from the wall (figure 5). This allows for stronger forcing of the normal vorticity equation, and larger coupling is expected. Meanwhile, in zero and favourable pressure gradient, the maximum shear is concentrated close to the wall. The forcing to the Squire equation is therefore limited, especially since the weighting function, $\phi(y)$, satisfies the no-slip condition, $\phi = 0$, at the wall.

The solution to the initial-value problem of the Squire response to Orr–Sommerfeld mode forcing is given in Zaki & Durbin (2005). A single Orr–Sommerfeld mode, $(\tilde{k}_y; k_x, k_z)$, was considered; the tilde distinguishes the wall-normal wavenumber of the forcing mode because the Squire response is a spectrum in k_y. The vertical velocity disturbance is given by

$$v(\boldsymbol{x}, t) = a_0 \phi(y) \exp\left(\mathrm{i}\left(k_x x + k_z z - \omega_{os,\tilde{k}_y} t\right)\right). \tag{4.1}$$

The Squire response is expanded in terms of the discrete and continuous eigenfunctions of its homogeneous operator,

$$\eta_{\boldsymbol{\kappa}}(y, t) = \sum_{n=1}^{N_{SQ}} b_n(t) \chi_n(y) + \int_{k_y} b_{k_y}(t) \chi_{k_y}(y)\, \mathrm{d}k_y, \tag{4.2}$$

where $\boldsymbol{\kappa}$ is the horizontal wavenumber vector (k_x, k_z), and

$$\eta_{\boldsymbol{\kappa}}(y, t) = \int_{k_x} \int_{k_z} \eta(\boldsymbol{x}, t) \exp(-\mathrm{i}k_x x) \exp(-\mathrm{i}k_z z)\, \mathrm{d}z\, \mathrm{d}x.$$

Subscript n denotes the discrete eigensolutions, while k_y refers to the continuous spectrum. An expression for the coefficients b_n and b_{k_y} can be obtained by making use of the orthogonality properties of the adjoint problem, namely

$$\langle \chi_m^\dagger, \chi_n \rangle = \delta_{mn}, \qquad \left\langle \chi_{k_y}^\dagger, \chi_{k_y'} \right\rangle = \delta(k_y - k_y'),$$

where the dagger marks the adjoint eigenfunctions, and the dot product is defined according to $\langle f, g \rangle \equiv \int_0^\infty f^* g\, \mathrm{d}y$. In evaluating b_{k_y}, it should be noted that exact resonance indeed exists between the continuous Orr–Sommerfeld and Squire eigensolutions at $k_y = \tilde{k}_y$; that is $\omega_{SQ}(k_y = \tilde{k}_y; k_x, k_z) = \omega_{OS}(\tilde{k}_y; k_x, k_z)$. Taking resonance into account, the spectral coefficients of the normal vorticity expansion are derived: for discrete Squire modes,

$$b_m(t) = b_m(0) \exp(-\mathrm{i}\omega_m t) - a_0 \langle \chi_m^\dagger, \mathscr{C}\phi(y) \rangle \left[\frac{\exp\left(-\mathrm{i}\omega_{os,\tilde{k}_y} t\right) - \exp(-\mathrm{i}\omega_m t)}{-\mathrm{i}\left(\omega_{os,\tilde{k}_y} - \omega_m\right)} \right]; \tag{4.3}$$

for continuous Squire modes $(k_y \neq \tilde{k}_y)$,

$$b_{k_y}(t) = b_{k_y}(0) \exp(-\mathrm{i}\omega_{k_y} t) - a_0 \left\langle \chi_{k_y}^\dagger, \mathscr{C}\phi(y) \right\rangle \left[\frac{\exp\left(-\mathrm{i}\omega_{os,\tilde{k}_y} t\right) - \exp\left(-\mathrm{i}\omega_{k_y} t\right)}{-\mathrm{i}\left(\omega_{os,\tilde{k}_y} - \omega_{k_y}\right)} \right]; \tag{4.4}$$

and for the resonant mode $(k_y = \tilde{k}_y)$,

$$b_{\tilde{k}_y}(t) = b_{\tilde{k}_y}(0) \exp\left(-\mathrm{i}\omega_{\tilde{k}_y} t\right) - a_0 \left\langle \chi_{\tilde{k}_y}^\dagger, \mathscr{C}\phi(y) \right\rangle t \left[\exp\left(-\mathrm{i}\omega_{os,\tilde{k}_y} t\right) \right]. \tag{4.5}$$

In the absence of any initial vertical vorticity, $\eta_{\boldsymbol{\kappa}}(y, t = 0) = 0$, the initial values of the coefficients vanish, $b_m(0) = b_{k_y}(0) = 0$.

The Squire response was evaluated numerically for forcing by a single Orr–Sommerfeld mode $k_x = 10^{-2}$, $k_y = \{\pi/2, \pi, 2\pi\}$, $k_z = \pi$. The results at the time of

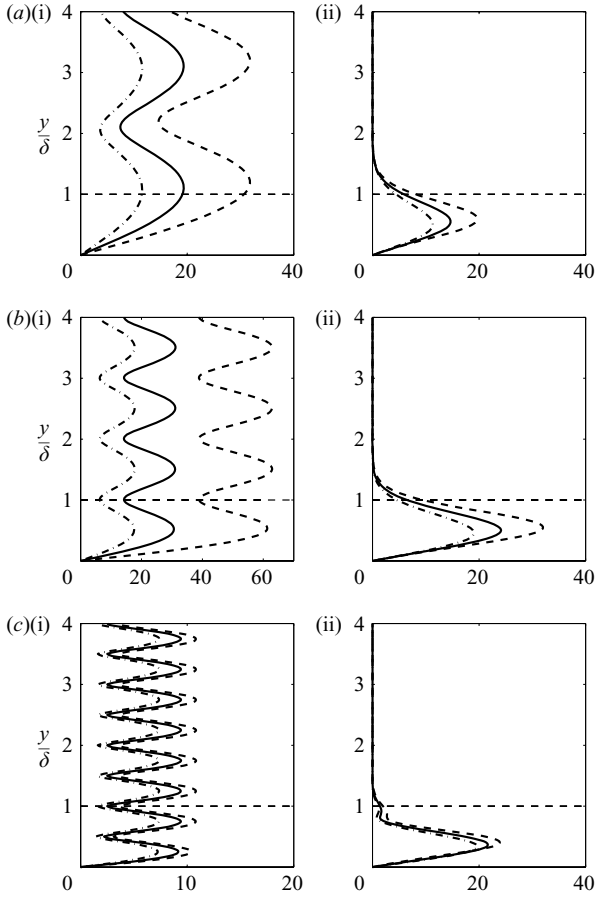

FIGURE 7. Squire response to Orr–Sommerfeld forcing at $R = 10^3$, $k_x = 10^{-2}$, $k_z = \pi$, $k_y = \{\pi/2, \pi, 2\pi\}$. The solution is plotted at the time where η reaches its maximum amplitude, prior to viscous decay. (i) The resonant term of Squire response, $b_{\kappa,\tilde{k}_y}\chi_{\kappa,\tilde{k}_y}(y)$; (ii) the full solution (4.2). — · —, $\beta = +0.5$; ——, $\beta = 0$; - - -, $\beta = -0.18$. (*a*) $k_y = \pi/2$, (*b*) $k_y = \pi$, (*c*) $k_y = 2\pi$.

maximum normal-vorticity response are shown in figure 7. The resonant term in the expansion (4.2) is shown in figure 7(i). Clearly, it reaches higher amplitude for the APG case, followed by the zero, and favourable pressure gradients. The same trend is observed in the full solution, in figure 7(ii). The enhanced coupling, or stronger perturbation jets in retarded flows, could be a cause of earlier transition onset. Meanwhile, weak coupling in accelerated flows could delay transition.

The presence of pressure gradient has little effect on the vertical location of the maximum normal vorticity perturbation. In the case of APG, the maximum is located higher in the boundary layer. However, this effect is secondary. It is more interesting to examine the effect of $\tilde{k}_y$ on the location of the peak in the response. While the peak in the resonant response shifts with varying $\tilde{k}_y$, the full superposition of Squire modes peaks near the middle of the boundary layer. This is in agreement with experimental observation, where the shape of Klebanoff distortion is found to have little dependence on the free-stream turbulence characteristics (Westin *et al.* 1994).

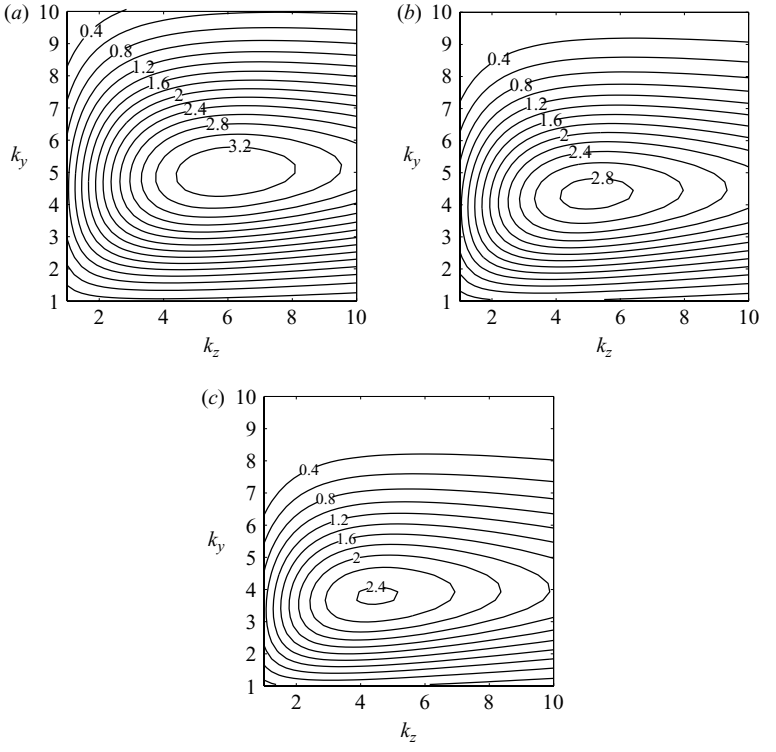

FIGURE 8. The coupling coefficient for $R = 100$, $k_x = \pi/10$ in (a) adverse, (b) zero, and (c) favourable pressure gradient; $\beta = \{-0.18, 0.0, +0.50\}$. Contour levels start at $\Theta = 0.4$ and are incremented by 0.2.

5. Mode coupling

In order to characterize the ability of Orr–Sommerfeld modes to generate boundary-layer streaks, Zaki & Durbin (2005) proposed a coupling coefficient,

$$\Theta \equiv \left| \frac{-\mathrm{i}\langle \chi^\dagger, \mathscr{C}\phi \rangle}{\omega_{os}^i} \right| = \left| k_z \frac{\langle \chi^\dagger, U'\phi \rangle}{\omega_{os}^i} \right|, \tag{5.1}$$

where the eigenfunctions are normalized to unit maximum amplitude in the free stream. The coupling coefficient is non-zero only for three-dimensional Orr–Sommerfeld modes. It accounts for the variation of modal penetration depth and for the distribution of mean shear in the boundary layer. Finally, since the streaks initially intensify, but then decay viscously, the coefficient is scaled by the decay rate ω^i. This ensures that the coefficient disfavours quickly decaying modes, even if they penetrate the boundary layer; such is the case of high k_y disturbances.

Figures 8(a) to 8(c) show the coupling coefficient in adverse, zero and favourable pressure gradients for $k_x = \pi/10$, $R = 10^2$. In each of the figures, the maximum Θ is achieved at $k_y \sim O(\pi)$ and $k_z \sim O(2\pi)$. This value of k_z is similar to the spanwise scale of boundary-layer streaks, $\lambda_z \sim O(\delta)$, observed in experiments and DNS of bypass transition (Kendall 1985; Jacobs & Durbin 2000). The preferred spanwise scale can be explained by recognizing that increasing k_z has the dual effect of enhancing the forcing to the Squire operator, but also increasing the viscous decay rate. As a result, in the presence of a spectrum of free-stream vortical disturbances, the preferred

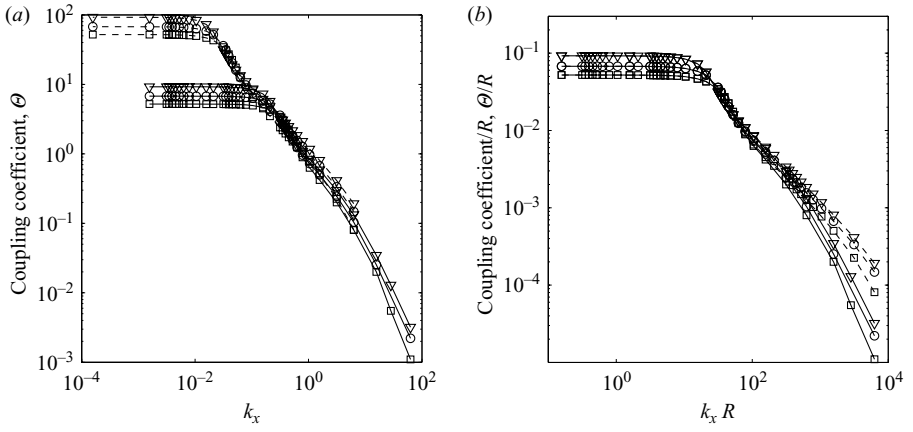

FIGURE 9. The optimal coupling coefficient, for - - -, $R = 10^3$, and ——, $R = 10^2$. Symbols correspond to pressure gradient parameters, □, FPG $\beta = 0.50$; ○, ZPG $\beta = 0$; ▽, APG $\beta = -0.18$.

spanwise wavenumber, $k_z \sim O(2\pi)$ is dominant: smaller scales viscously decay, and larger scales are weaker forcing to the Squire equation.

The preferred wall-normal scale, $\lambda_y \sim O(2\delta)$, has not been directly addressed in the literature. The importance of documenting the anisotropy of the free stream has been recognized (see for example Westin *et al.* 1994). However, a preferred wall-normal wavenumber has not been identified. The preferred wall-normal scale predicted by the maximum in the coupling coefficient is of the order of the boundary-layer thickness. Larger λ_y eigenfunctions are expelled by the boundary-layer shear (recall from § 3 that penetration into the boundary layer is proportional to $1/\lambda_y^2$). Perturbations of smaller vertical scale are subject to high viscous decay rates and, as a result, do not persist at long times in the temporal problem, or far downstream of the leading edge in the spatial equivalent.

The maximum Θ decreases from adverse (figure 8*a*) to zero (figure 8*b*), and finally to favourable pressure gradient (figure 8*c*). This trend is consistent with the initial-value problem. Also, the location of the maximum shifts in (k_y, k_z)-space. This shift is due to the variation in shear sheltering of the mean profiles.

Figure 9 illustrates the value of Θ at the optimal (k_y, k_z) for a range of $k_x R$. For $k_x R > 10$, the coupling coefficient is decreasing because of enhanced shear sheltering of high-frequency modes, particularly at large Reynolds number. The increase in sheltering limits penetration of the Orr–Sommerfeld modes into the boundary layer, and hence reduces coupling to the boundary-layer shear. For $k_x R < 10$, the Orr–Sommerfeld modes are fully penetrating. As a result, the coupling coefficient is maximum. The coefficient scales linearly with Reynolds number owing to the modal decay rate, $\omega_i \propto 1/R$, in the denominator of Θ. The linear dependence on R causes the curves of Θ/R to collapse in figure 9(*b*).

The effect of pressure gradient on Θ is also demonstrated in figure 9. Adverse pressure gradient improves coupling. This is consistent with the initial-value problem, which motivates the definition of Θ. Orr–Sommerfeld modes with large coupling are penetrating, and have low decay rates. As a result, they force strong boundary-layer streaks which persist for long times (or far downstream in the spatial problem). The

propensity of the Orr–Sommerfeld mode to generate the perturbation jets is enhanced in retarded flows; this is captured by the coupling coefficient.

6. Direct numerical simulations

This section describes direct numerical simulations (DNS) of boundary layers perturbed by single or pairs of inflow Orr–Sommerfeld modes. The modal interaction and coupling to the boundary-layer shear are investigated, with particular emphasis on the effect of pressure gradients. The inflow perturbations used in the simulations are based on the spatial eigenvalue problem. First, a single penetrating Orr–Sommerfeld mode is simulated in order to verify the conclusions of linear theory. Then, pairwise mode interactions are presented.

A schematic of the computational domain is shown in figure 1. The domain boundaries are marked by the dashed line. The domain height is large enough to ensure that the boundary layer on the lower plate is unaffected by the boundary conditions at the top surface. The size of the domain, scaled by the inflow boundary-layer thickness, δ_0, is $400 \times 20 \times 16$ in the streamwise, wall-normal and spanwise directions, respectively. The grid resolution corresponds to that of Jacobs & Durbin (2000), who performed extensive refinement studies. A total of 26 million mesh points are used to capture the three-dimensional transition.

The computational algorithm is based on a staggered grid with a local volume flux formulation in curvilinear coordinates (Rosenfeld, Kwak & Vinokur 1991; Wu & Durbin 2001). Adams–Bashforth is implemented for the explicit time advancement of convective terms. Pressure and diffusion are treated by implicit Euler and by Crank–Nicolson, respectively.

The top boundary of the computational domain is a free-slip surface, which is contoured in order to induce the desired streamwise pressure distribution. Here, it is designed to produce a power-law acceleration of the free stream and, as a result, a constant value of the Falkner–Skan parameter β, which can be directly related to the pressure gradient parameter $\lambda_\theta \equiv (\theta^2/\nu)\,\mathrm{d}U_\infty/\mathrm{d}x$.

In all the simulations, independent of the streamwise pressure distribution, a Blasius mean velocity profile is prescribed at the inflow. Inflow perturbations are also based on the zero pressure gradient Blasius profile. This choice circumvents ambiguities which would arise if a Falkner–Skan mean velocity and associated Orr–Sommerfeld modes were imposed: First, for Falkner–Skan mean profiles, the origin of the flow is fictitious and is a function of the pressure gradient parameter. As a result, even for the same inlet Reynolds number R, the inflow location would seem to vary artificially among simulations because it is measured with respect to a fictitious origin. Also, the shape of the inflow Orr–Sommerfeld perturbation would vary among simulations because it is a function of the inflow mean velocity profile. Particularly, modes with the same amplitude in the free stream would be different at the edge of the boundary layer.

In order to eliminate those ambiguities, the inflow is chosen to be the Blasius mean profile, plus a disturbance corresponding to the ZPG mode. This approach allows for direct comparison between the results in different pressure gradients. The effect of the pressure gradient on mode shape is therefore a consequence of solving the full Navier–Stokes equations within the computational domain, and not imposed as an inflow boundary condition.

A convective outflow condition is used. We found no upstream contamination, so this was deemed satisfactory for present purposes.

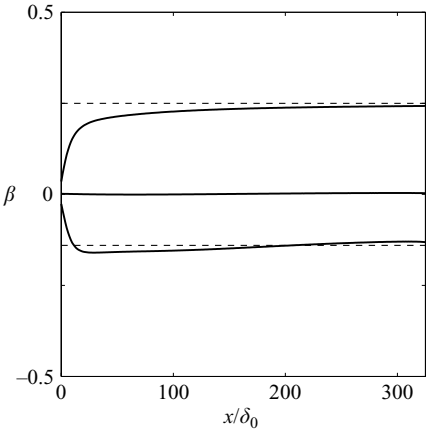

FIGURE 10. The Falkner–Skan parameter, β evaluated from a laminar solution. Solid lines show the computed β, and the dashed lines the design values.

A disturbance-free laminar solution is first obtained in order to verify the pressure gradient level throughout the domain. The results are illustrated in figure 10. The pressure gradient adjusts quickly to the design values $\beta = \{-0.14, 0, 0.25\}$. Those levels are then maintained throughout the domain. The pressure gradient parameter was also computed from the time-averaged results in all the following DNS. It closely matched the design values throughout the domain in the non-transitional computations. In simulations yielding transition, the desired pressure gradient was maintained upstream of the turbulent boundary layer.

6.1. *Effect of mean pressure gradient on mode coupling*

The effect of pressure gradient on the intensity of Klebanoff distortions was discussed previously from the perspective of the initial-value problem. Flow deceleration was found to enhance coupling between the low-frequency vortical disturbances and the boundary-layer shear. However, nonparallel effects and nonlinearity were ignored in that analysis. Both aspects are important: the former is relevant in discussing the behaviour of low-frequency perturbations; the latter is significant owing to the large amplitude of the boundary-layer response.

In the simulations, a single penetrating Orr–Sommerfeld mode is prescribed at the inflow of the computational domain. The spatial evolution of the disturbance and the boundary-layer response are obtained by solving the full Navier–Stokes equations: both non-parallel effects and nonlinearity are therefore fully represented.

The inflow mode $\omega = 10^{-2}$, $k_y = \pi$, $k_z = \pi/2$ is shown in figure 11. This low-frequency disturbance clearly penetrates into the boundary layer. The root mean square of the free-stream vertical velocity perturbation is prescribed at the inflow of the computational domain, $v_{rms} = 0.55\,\%$. Three direct numerical simulations were carried out, corresponding to pressure gradient parameters $\beta = \{-0.14, 0.0, +0.25\}$. The coupling coefficients at these three values of β are, respectively, $\Theta = \{56.7, 48.1, 41.6\}$. Since the inflow is identical in all three simulations, the variation in coupling emerges downstream owing to the applied pressure gradient, and is not due to the inflow mean profile or perturbation.

The study of continuous Orr–Sommerfeld mode coupling bears on the intensity of the boundary-layer perturbation jets. While the vertical and spanwise disturbance velocities are of the same order as the free-stream perturbation, the streamwise velocity

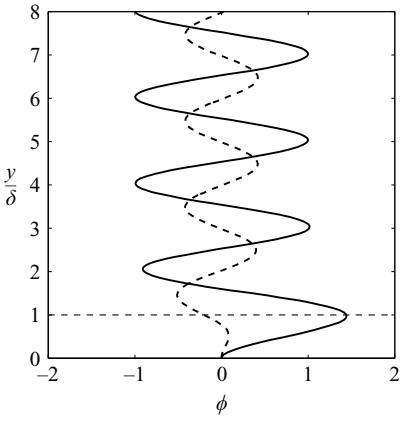

FIGURE 11. Orr–Sommerfeld inflow mode shape: $R = 10^3$, $\omega = 10^{-2}$, $k_y = \pi$, $k_z = \pi/2$. The solid line is the real part of the eigenfunction, and the dashed line the imaginary component.

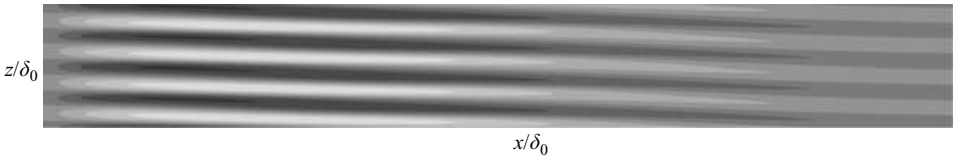

FIGURE 12. Instantaneous contours of streamwise velocity fluctuation ($-0.3 \leqslant u \leqslant 0.3$) evaluated at $y/\delta_0 = 0.5$. The streamwise extent shown is $0.4 \times 10^5 \leqslant R_x \leqslant 3.5 \times 10^5$. The spanwise coordinate $0 \leqslant z \leqslant 16$ is enlarged by a factor of 3. Inlet mode: $\omega = 0.01$, $k_y = \pi$, $k_z = \pi/2$.

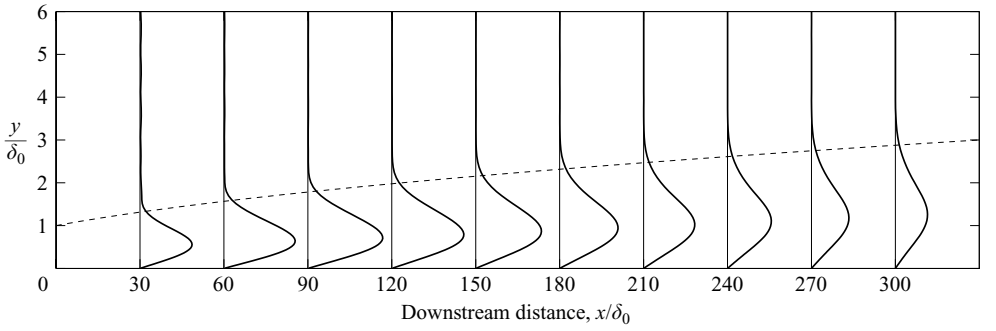

FIGURE 13. Vertical profiles of u_{rms} at various x-locations. The dashed line shows the edge of the boundary layer.

reaches high amplitudes inside the boundary layer. Those elongated disturbances initially intensify owing to tilting of the mean shear by the Orr–Sommerfeld mode. Farther downstream, viscosity becomes dominant and the perturbation jets decay.

This behaviour is clear in the instantaneous field of figure 12 from the zero pressure gradient simulation. The plan view shows contours of streamwise velocity perturbation. The root mean square streamwise disturbance is shown in figure 13, at different x-locations. The disturbance has the shape of a Klebanoff distortion, and is similar in form to the solution of the initial-value problem. The mode amplification and the subsequent viscous decay are captured in the figure.

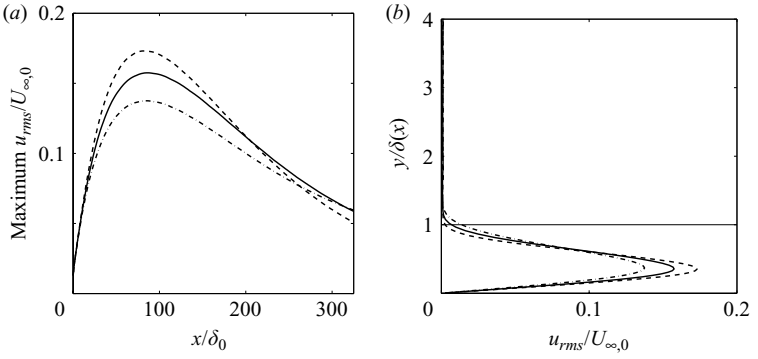

FIGURE 14. (*a*) The maximum u_{rms} versus downstream distance. (*b*) The perturbation profile at the x-location where u_{rms} reaches its maximum value. — · —, $\beta = +0.25$; ——, $\beta = 0.0$; - - -, $\beta = -0.14$.

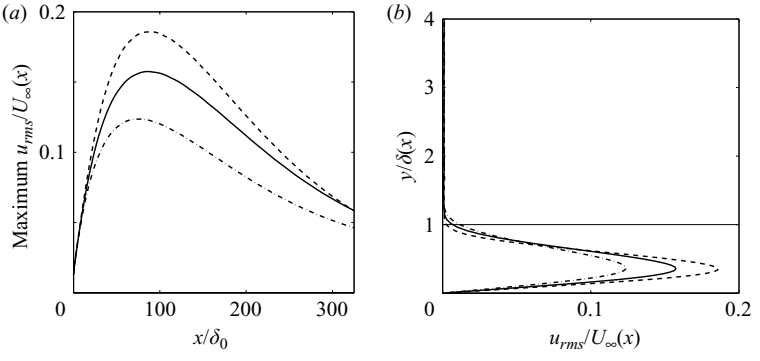

FIGURE 15. (*a*) The maximum $u_{rms}/U_\infty(x)$ versus downstream distance. (*b*) The perturbation profile at the x-location where $u_{rms}/U_\infty(x)$ reaches its maximum value. — · —, $\beta = +0.25$; ——, $\beta = 0.0$; - - -, $\beta = -0.14$.

The maximum r.m.s. streamwise velocity disturbance can be obtained at every x-location, and is shown in figure 14(*a*). The DNS confirm the prediction of linear theory: penetrating Orr–Sommerfeld modes induce stronger boundary-layer perturbation jets in APG owing to improved coupling. The location of the maximum is $x \simeq 80$ in all cases.

Figure 14(*b*) shows the shape of the Klebanoff distortion at the location of maximum response, prior to the onset of viscous decay. The shape of the response is little affected by the mean flow acceleration. Only the amplitude of the boundary-layer streaks is enhanced by adverse pressure gradient. Qualitatively, the mode shape agrees with the superposition of Squire eigenfunctions in the solution to the initial-value problem. In particular, the location of the maxima, midway through the boundary layer, is consistent with the prediction of linear theory. This observation is also in agreement with Westin *et al.* (1994), where the location of the maximum in Klebanoff modes was recorded midway in the boundary layer, independent of the streak intensity.

The r.m.s. disturbances presented in figure 14 are non-dimensionalized by the inflow free-stream velocity, $U_\infty(x_0)$. The effect of pressure gradient on the intensity of streaks is amplified when the local free-stream velocity, $U_\infty(x)$ is used for scaling, as in figure 15. Local scaling is relevant because, in the case of a fully turbulent

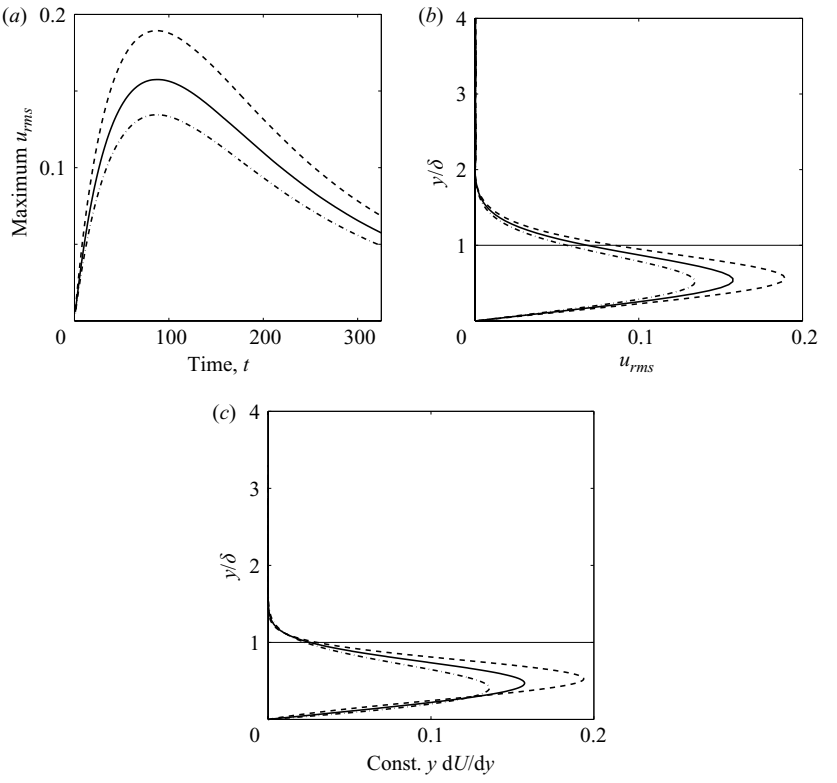

FIGURE 16. Prediction of linear theory. All three curves are scaled by the same multiplicative factor which is chosen such that the maximum amplitude of the ZPG case matches that of DNS. (*b*) The mode shape at the time when u_{rms} reaches its maximum value. (*c*) $y\,\mathrm{d}U/\mathrm{d}y$, also pre-multiplied by a scaling constant in order to match the DNS amplitude for the ZPG simulation. — · —, $\beta = +0.25$; ——, $\beta = 0.0$; - - -, $\beta = -0.14$.

free stream, bypass transition of the streaky boundary layer is produced by localized forcing from above. Instabilities are triggered *locally*, at the edge of the boundary layer, where perturbation jets are exposed to the high-frequency non-penetrating free-stream disturbances.

The solution to the initial-value problem presented earlier neglects both non-parallel and nonlinear effects. Therefore, it cannot be expected that linear theory predicts the correct amplitude of the boundary-layer response. However, whether linear theory can capture the effect of pressure gradient on the solution is worth investigating. To this end, the results of the IVP are rescaled in order to match the maximum amplitude of the Klebanoff distortion from the DNS in zero pressure gradient. Figure 16 shows the scaled prediction of linear theory. The figure demonstrates that linear theory captures the dependence on pressure gradient, and the results based on the coupling coefficient are reliable in assessing the effect of flow acceleration on coupling. Figure 16(*c*) shows $y\,\mathrm{d}U/\mathrm{d}y$, also scaled in order to match the DNS in ZPG. The approximation gives a good representation of the shape of Klebanoff modes. However, it does not carry any information regarding the effect of the length scale of the inflow mode. The coupling coefficient, based on the initial-value problem, includes such information.

The disturbance growth and decay in figures 14 and 15 are qualitatively similar to the results of Lasseigne *et al.* (1999) for an inflow disturbance that attains maximum

energy amplification. The resemblance is not surprising: the optimal disturbance of Lasseigne *et al.* (1999), when expanded in terms of the Orr–Sommerfeld eigenbasis, is composed of low-frequency modes, similar to the inflow mode in our DNS. Since the Orr–Sommerfeld eigenfunctions form a complete basis, and are derived from the linear perturbation equations (Grosch & Salwen 1978), they provide a natural basis for expanding any general disturbance and evaluating the influence of its spectral constituents on the boundary layer. In particular, the continuous modes, which are oscillatory in the free stream, can unambiguously be applied in the spectral decomposition of free-stream turbulence interacting with the boundary layer in bypass transition (Jacobs & Durbin 2000).

In this section, the influence of pressure gradient on the intensity of boundary-layer streaks was computed using DNS: APG enhances the intensity of Klebanoff distortions, while FPG reduces coupling and, as a result, the intensity of streaks. All of the non-linear simulations of low-frequency inflow modes predicted viscous decay of Klebanoff distortions at large downstream distances. The viscous decay implies that Klebanoff distortions, *per se*, are insufficient for transition to take place. A breakdown mechanism is required in order to trigger the formation of turbulent spots and transition to turbulence. This mechanism was suggested in Wu *et al.* (1999) and Jacobs & Durbin (2000), and verified by Zaki & Durbin (2005) in the framework of continuous mode transition due to bimodal interaction. In that framework, boundary-layer streaks are generated owing to a single inflow low-frequency Orr–Sommerfeld disturbance. A sheltered high-frequency Orr–Sommerfeld mode is also included at the inlet. This mode triggers the instability and breakdown of the lifted streaks near the free stream. In continuous mode transition, the streaks need not be induced by inflow disturbances that cause maximum energy growth. A strongly coupled Orr–Sommerfeld eigenfunction is sufficient.

Provided a breakdown mechanism is present, one important question must be addressed: Does the intensity of the perturbation jets correlate with transition location? Westin *et al.* (1994) argue that such correlation is weak. However, the experiments they cited had different turbulent free streams, and different leading-edge conditions. They recognized these caveats. In the next section, we show in the framework of continuous mode transition that such correlation does exist. A minimal level of streak intensity is demonstrated necessary for spot inception and transition. Furthermore, higher-intensity boundary-layer perturbation jets are more susceptible to instability when exposed to forcing by the free-stream high-frequency disturbances. As a result, transition occurs earlier upstream for stronger Klebanoff modes. This hypothesis is first verified in zero pressure gradient, and the results applied to explain the effect of pressure gradients on transition onset.

6.2. *Bimodal interaction, and continuous mode transition*

The term ‘bypass transition’ refers to the process by which free-stream vortical disturbances induce transition to turbulence in an underlying boundary layer, without the intervention of Tollmien–Schlichting instability waves. Linear theory has provided insight into the ability of low-frequency vortical disturbances to penetrate the boundary layer and generate Klebanoff distortions. The next stage of the bypass process is breakdown to turbulence, a complex phenomenon not amenable to linear analysis. In fact, one interpretation of the terminology ‘bypass transition’ is that the mechanism bypasses any theoretical explanation (Morkovin 1969). In the title to the present paper, we use the term ‘continuous mode transition’ because the present simulations study bypass transition by starting with continuous modes at the inlet. This provides a natural complement to orderly transition, proceeding from discrete mode evolution.

Zaki & Durbin (2005) demonstrated that the entire transition process can be realized through the interaction of a pair of Orr–Sommerfeld continuous modes: one low-frequency penetrating mode and one high-frequency sheltered eigenfunction. The penetrating three-dimensional Orr–Sommerfeld mode resonantly forces the Squire operator. The response, a superposition of Squire modes, results in boundary-layer streaks. While this is a route into the boundary layer, transition subsequently involves an interaction between low- and high-frequency modes. The backward jets, induced by upward displacement of mean momentum, are lifted towards the edge of the boundary layer. The streaky boundary-layer profile becomes susceptible to an inflectional type instability when exposed to the high-frequency non-penetrating disturbance in the free stream. The growing instabilities are the onset of breakdown, near the top of the boundary layer. This process defines continuous mode transition – as an instance of the bypass route to turbulence.

The role of pressure gradient in continuous mode transition must be, by definition, independent of the Tollmien–Schlichting instabilities of the mean velocity profile, which are characteristic of natural transition. Instead, the dependence of the lifted streak intensity on mean pressure gradient becomes important. In adverse pressure gradient, enhanced intensity of the perturbation jets, particularly based on local scaling, could account for earlier transition. Similarly, weak Klebanoff distortions in accelerated flows could contribute to the delayed transition onset. However, before these assertions can be made regarding transition in accelerated flows, the effect of streak intensity on transition location should be verified in zero pressure gradient.

DNS were performed under zero-pressure-gradient conditions with only two modes at the inflow: a low- and a high-frequency perturbation. The inflow boundary condition is given according to

$$\boldsymbol{u}_{inflow} = \boldsymbol{U}_{Blasius} + \sum_{j=1}^{2} \epsilon_j \,\mathrm{Re}\left\{ \frac{1}{k_x^2 + k_z^2} \begin{bmatrix} \mathrm{i}k_x \,\mathrm{d}\phi_j/\mathrm{d}y \\ \left(k_x^2 + k_z^2\right)\phi_j \\ \mathrm{i}k_z \,\mathrm{d}\phi_j/\mathrm{d}y \end{bmatrix} \exp(\mathrm{i}(\pm k_z z - \omega t)) \right\}.$$

The modes are indexed by $\{j; k_z, k_y, \omega\}$. For the base case, the amplitude of each inflow mode was normalized such that $v_{rms} = 3\,\%$ in the free stream. The amplitude of the low-frequency mode was then changed while holding that of the high-frequency inflow disturbance constant. If there exists an intensity at which perturbation jets first become susceptible to high-frequency instability, this threshold might not be reached in the case of lower amplitudes of the inflow. Transition will therefore be suppressed. Meanwhile, for higher inflow amplitude, the magnitude of the Klebanoff distortion is enhanced. If stronger perturbation jets are more susceptible to instability, transition will be observed earlier upstream. It should also be noted that, at upstream locations, the magnitude of the sheltered high-frequency disturbance has not decayed substantially. Therefore, the high-frequency disturbance can strongly destabilize the lifted boundary-layer streaks.

Figure 17 shows the time-averaged skin friction curves for three magnitudes of the low-frequency inflow mode, $v_{rms} = \{2\,\%, 3\,\%, 4\,\%\}$. The case of lowest inflow intensity does not undergo transition within the computational domain. The other two cases transition, with the highest inflow intensity case reaching a fully turbulent condition at the earliest point upstream. Other simulations for different inflow mode pairs show similar trends.

Figure 18 shows the maximum r.m.s. streamwise perturbation as a function of downstream distance. The three curves correspond to the different inflow amplitudes

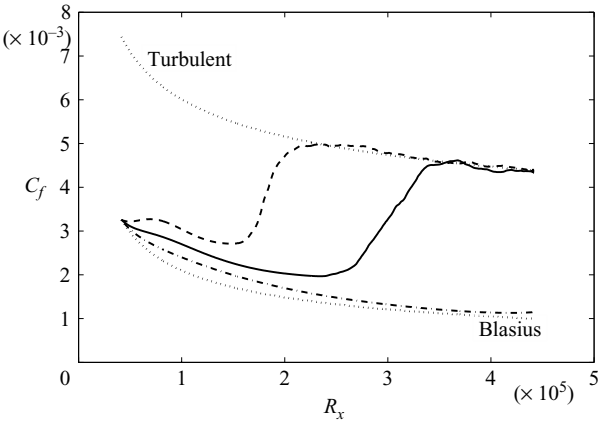

FIGURE 17. Time-averaged skin friction profiles. Inlet modes: $\omega = \pi/100$, $k_y = 2\pi/3.2$, $k_z = 2\pi/3.2$, $\Theta = 19.3$ and $\omega = \pi/10$, $k_y = 2\pi/3$, $k_z = 2.75$, $\Theta = 1.34$. Three amplitudes of the inlet low-frequency disturbance are shown: — · —, $v_{rms} = 2.0\,\%$; ——, $v_{rms} = 3.0\,\%$; - - -, $v_{rms} = 4.0\,\%$.

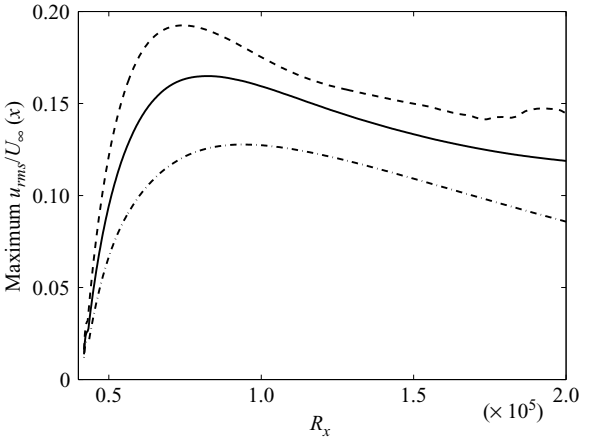

FIGURE 18. The maximum u_{rms} versus downstream distance. Three amplitudes of the inlet low-frequency disturbance are shown: — · —, $v_{rms} = 2.0\,\%$; ——, $v_{rms} = 3.0\,\%$; - - -, $v_{rms} = 4.0\,\%$.

of the low-frequency mode. As expected, the Klebanoff distortion is strongest for the highest inflow amplitude; this simulation transitions at the earliest point upstream. Meanwhile, for the lowest inflow amplitude, the boundary-layer streaks are weakest, and transition is absent from the computational domain.

In bypass transition due to free-stream turbulence, the amplitude of Klebanoff distortions scales linearly with the free-stream intensity (Kendall 1985). That linear dependence is not observed in our simulations (see figure 18) because in continuous mode transition, the dominant disturbance inside the boundary layer is the response to a single low-frequency Orr–Sommerfeld eigenfunction, and not an entire spectrum of disturbances. Therefore, a linear dependence of streak intensity on the single low-frequency inflow mode is only possible for small perturbations, or in the linear limit. The amplitudes of the disturbances considered here are, however, beyond the linear

regime. This large amplitude is necessary in order to generate boundary-layer streaks that are of similar intensities to those in bypass transition owing to fully turbulent free streams, but using a single low-frequency inlet mode.

The controlled numerical experiments described here clearly identify a connection between the intensity of perturbation jets in the laminar layer and the location of transition (figures 17 and 18). These simulations are particularly important for two reasons. First, only two inlet O-S modes are used to trigger the entire transition process. Unlike a fully turbulent free stream, the small and large disturbance scales become distinctly separated and their roles clearly discernible. Secondly, there is no leading-edge effect. Therefore, the relation between the free-stream turbulence length scale and leading-edge diameter does not 'contaminate' the findings. Both experiments and computer simulations support our approach of starting downstream of the leading edge: Kendall (1991) observed that the development of Klebanoff distortions is insensitive to the aspect ratio of his elliptical leading edge. Meanwhile, he reported a nonlinear increase in the amplitude of Tollmien–Schlichting instability waves with decreasing leading-edge aspect ratio. Nagarajan, Lele & Ferziger (2006) also investigated the effect of the leading-edge geometry using large-eddy simulations (LES). In the case of a blunt leading edge, they observed the generation of packets of instability waves, which can alter the transition mechanism. These packets are sporadic, and their origin remains unexplained. However, for a slender leading edge, bypass transition becomes independent of the leading-edge geometry, and is due to breakdown of the lifted boundary-layer streaks, or Klebanoff distortions. By eliminating the leading edge, transition in our simulations is not affected by receptivity to Tollmien–Schlichting waves: breakdown is solely due to continuous mode interaction. This breakdown mechanism is dominant when the leading edge is fine, or slender, compared to the free-stream turbulence length scale (Kendall 1991; Nagarajan *et al.* 2004).

The results from the zero-pressure-gradient simulations (figures 17 and 18) support the view that a stability threshold exists for the amplitude of lifted perturbations jets. This level is not reached in the case of low-amplitude inflow; the flow remains laminar throughout the computational domain. The simulations also confirm that stronger boundary-layer streaks are more susceptible to instability when exposed to the high-frequency free-stream disturbance. Now, this knowledge can be applied to the problem of continuous mode transition in pressure gradient.

Accelerated flows have weak coupling, and therefore low streak intensity. This effect is stabilizing: transition is either delayed or suppressed. On the other hand, retarded flows induce stronger perturbation jets and, as a result, are more susceptible to instability than zero-pressure-gradient boundary layers.

Pairwise mode interactions were simulated for accelerated and retarded mean flows. The inflow was identical among simulations. Only the top boundary condition was altered in order to achieve the desired mean pressure gradient. The effect of pressure gradient on continuous mode transition is shown in figure 19, where the time-averaged skin-friction profiles are plotted versus the downstream Reynolds number. Both C_f and R_x are defined using the free-stream velocity at the inflow plane. In the absence of pressure gradient, the skin friction curve follows the Blasius predicted value prior to transition, and the turbulent correlation downstream of the transitional region. The skin friction curve for the pressure gradient cases starts at the Blasius value because that is the inlet condition. Farther downstream, the skin friction curve shifts down for adverse, and up for favourable pressure gradient. The onset of transition is earliest upstream in adverse pressure gradient. Transition takes place farther downstream in the absence of pressure gradient, and is not observed within the computational

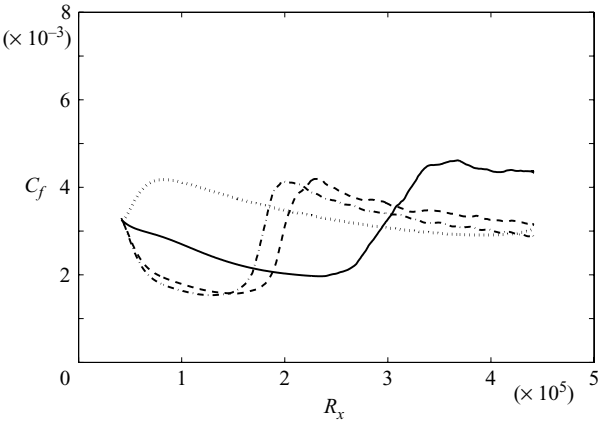

FIGURE 19. Time-averaged skin-friction profiles. Same inlet modes as in figure 17. Four values of the pressure gradient parameter are shown: ····, $\beta = +0.25$; ——, $\beta = 0.00$; - - -, $\beta = -0.14$; —·—, $\beta = -0.16$.

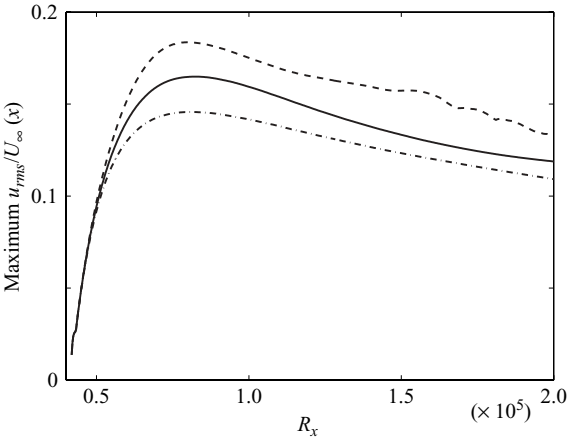

FIGURE 20. The maximum $u_{rms}/U_\infty(x)$ versus downstream distance. Three values of the pressure gradient parameter are shown: —·—, $\beta = +0.25$; ——, $\beta = 0.00$; - - -, $\beta = -0.16$.

domain in the case of accelerated flow. The results are in qualitative agreement with the experimentally observed trend (Abu-Ghannam & Shaw 1980).

Figure 20 shows the maximum root mean square streamwise velocity perturbation versus downstream distance. Here, u_{rms} is scaled by the local free-stream velocity. The trend showing stronger coupling for the APG simulation also persists if the inflow velocity is used for scaling. Enhanced streak intensity is clear for retarded flows. In contrast, the accelerated mean flow exhibits weaker perturbation jets than ZPG.

The effect of APG in figures 19 and 20 should be compared to the effect of increasing the amplitude of the low-frequency disturbance in figures 17 and 18. The results suggest both conditions enhance the amplitude of the perturbation jets and, as a result, cause early transition.

The transition length is shorter for both the APG cases than in ZPG. Shortening of transition length is also observed in the ZPG case when the inflow disturbance is of large amplitude. This, too, agrees qualitatively with Abu-Ghannam & Shaw (1980).

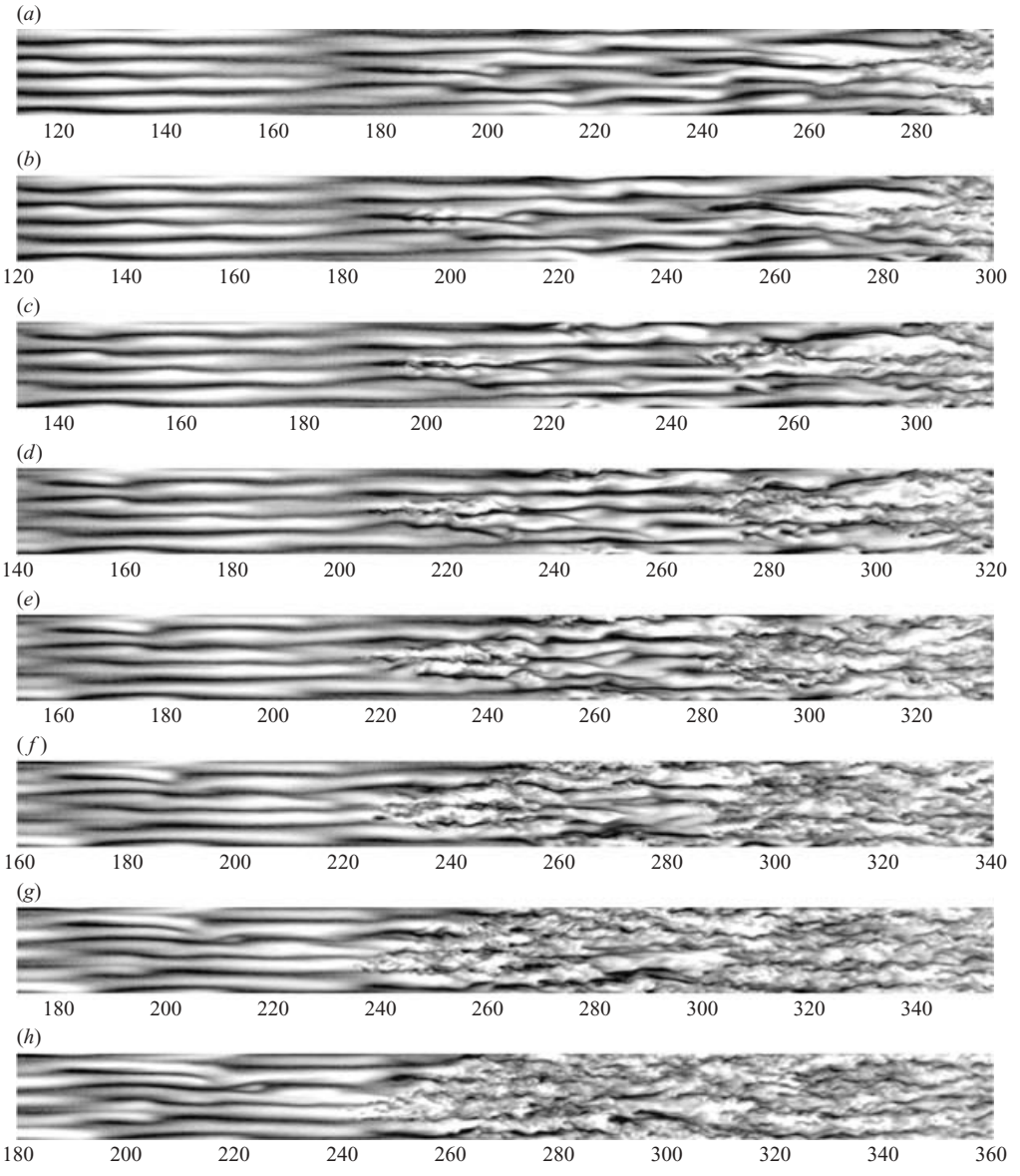

FIGURE 21. Instantaneous contours of streamwise velocity fluctuation ($-0.2 \leqslant u \leqslant 0.2$) in ZPG. The plane is located at $y/\delta_0 = 0.74$, and the frames translate in the flow direction at half the free-stream velocity.

The shorter transition length can be attributed to either an enhancement in spot formation rate, or faster spreading of the turbulent patches. The experimental literature supports the view that APG enhances both the inception and spreading rates of turbulent spots (Gostelow *et al.* 1994). Here, we compare the spreading of the patches in zero and adverse pressure gradient. A simple investigation of the time sequence showing the inception and evolution of turbulent spots can provide some insight.

Figures 21 and 22 are a time sequence showing spot formation. The former is the streamwise velocity fluctuation, and the latter the wall-normal component. The

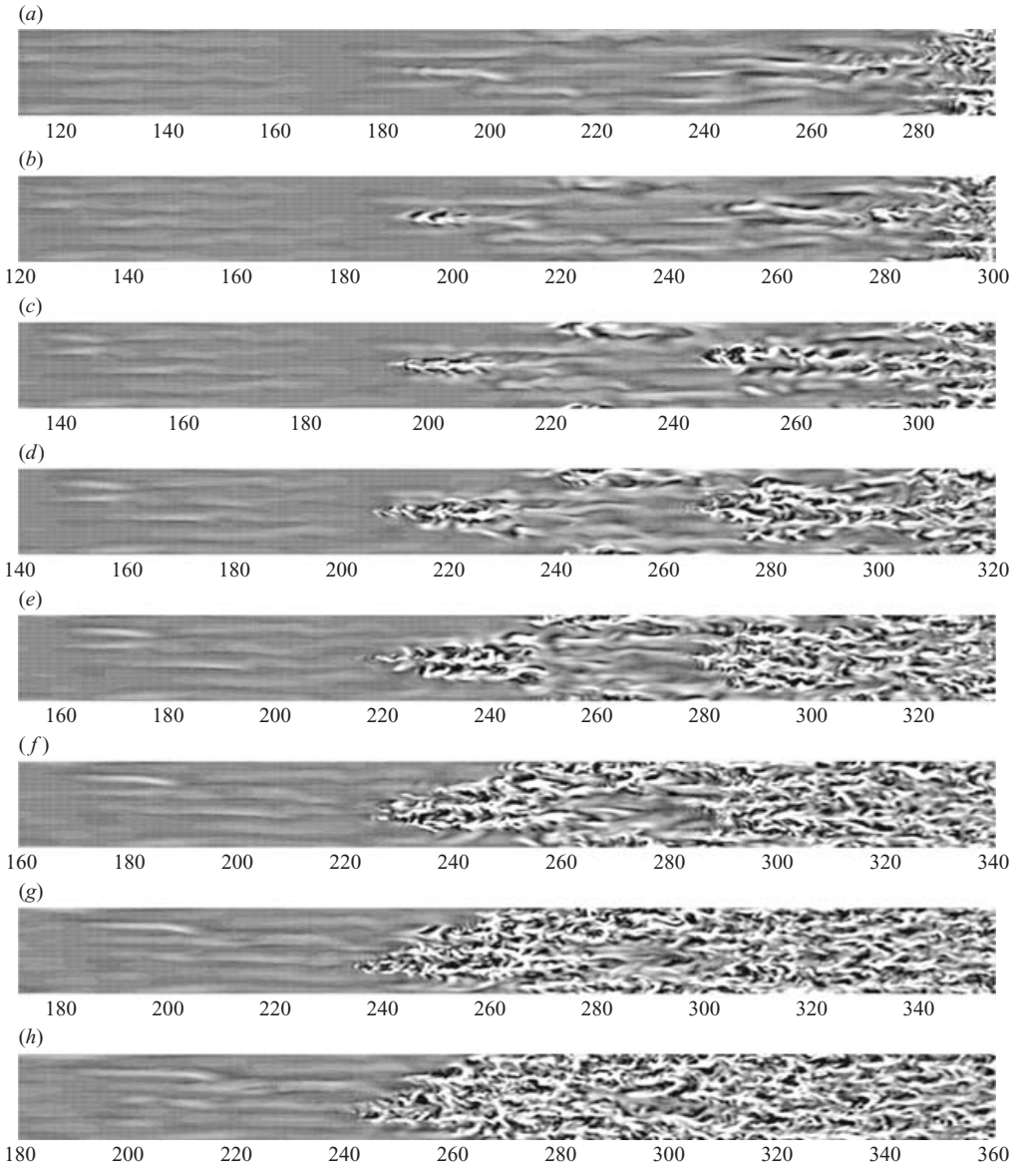

FIGURE 22. Instantaneous contours of wall-normal velocity fluctuation ($-0.05 \leqslant v \leqslant 0.05$) in ZPG. The plane is located at $y/\delta_0 = 0.74$, and the frames correspond to the same time instants as in figure 21.

frames translate to the right at half the free-stream velocity in order to keep the spot in the middle of each frame. Qualitatively, the figures agree with the time sequences reported by Jacobs & Durbin (2000). Three spots can be identified in the figures: one in the middle of the two-dimensional plane and two spots downstream, towards the edge of the periodic boundary and at mid-span, respectively. The spots are easily identified in the third frame. A laminar region separates the 'young' spots. As the turbulent patches convect downstream, they spread and finally coalesce into a fully turbulent boundary layer.

A few remarks are in order. First, in the absence of the high-frequency mode, the streaks decay viscously, and transition is not observed within the computational domain. The instability of the streaks occurs only if backward perturbation jets are exposed to high-frequency forcing when they lift-up and reach the edge of the boundary layer. Secondly, the spot inception is local, on single jets, as shown in figures 21 and 22. Spots are not preceded by a collective interaction of neighbouring streaks. However, once the instability of a particular streak grows, it contaminates neighbouring regions of the flow, and the spot spreads.

The instantaneous contours of velocity perturbations (figures 21 and 22) show a similarity to the images produced by Anthony, Jones & LaGraff (2005) with rapid response, heat transfer gauges. Anthony *et al.* (2005) observed that turbulent spots are initially composed of streamwise elongated structures, and noted that the patches of turbulence grow in size owing to the emergence of neighbouring heat flux streaks. Their observations are clearly in agreement with the time sequence presented here, particularly the streamwise velocity perturbation field (figure 21).

Figure 23 is a plan view of the instantaneous vertical velocity fluctuations close to the wall, at the same instants as in figure 22. The contour levels are an order of magnitude lower. The disturbance that presages a spot is weak in the first two frames of figure 23 and intensifies in the third. This can be contrasted to the behaviour away from the wall in figure 22: the disturbance that will spawn a spot has already reached high intensity in the second frame of the time sequence, twenty time units earlier than the plane close to the wall. This comparison confirms that the instability preceding spot inception occurs in the outer part of the boundary layer. Figure 24 provides further evidence in support of the location of spot inception. This figure is a zoomed-in side view of the breakdown seen in figures 21(*a*) and 21(*b*). The side view shows the wavy motion that leads to the occurrence of turbulent spots. The instability of the elevated shear regions clearly originates at the edge of the boundary layer. The near-wall region is insignificantly perturbed.

The instantaneous skin friction curves associated with transition are shown in figure 25. The curves are along a line bisecting the backward jet where the spots originates. The figure shows that the signature of the spot on the skin friction intensifies as the turbulent patch convects downstream. The laminar region that separates the young spot and the downstream turbulent boundary layer is also captured.

A good summary of all the above observations based on the ZPG simulation is presented in figure 26, which shows the streamwise perturbation energy decomposed into spanwise Fourier modes at various downstream Reynolds numbers. The fifth spanwise Fourier mode corresponds to $k_z = 2\pi/3.2$ of the penetrating inflow disturbance. Meanwhile, the seventh spanwise Fourier mode corresponds to $k_z = 2.75$ of the weakly coupled inflow disturbance. Figure 26(*a*) is a plane close to the wall, $y/\delta = 0.1$, and figure 26(*b*) is higher in the boundary layer, $y/\delta = 2/3$. At $y/\delta = 0.1$, only the fifth spanwise Fourier mode is observed to contain significant energy because only this disturbance penetrates the shear and generates the amplifying streaks. The weakly coupled perturbation does not penetrate and, hence, is absent from figure 26(*a*). In contrast, figure 26(*b*) shows both disturbances are present at $y/\delta = 2/3$, with the penetrating disturbance containing more energy. The tenth spanwise wavenumber, which corresponds to the first harmonic of the penetrating inflow mode, is also observed to emerge downstream, but decays prior to transition onset. The sudden cascade of energy among spanwise wavenumbers indicates breakdown to turbulence. This exchange clearly commences farther upstream in figure 26(*b*), away from the wall. This provides further evidence that transition commences towards the top of the boundary layer.

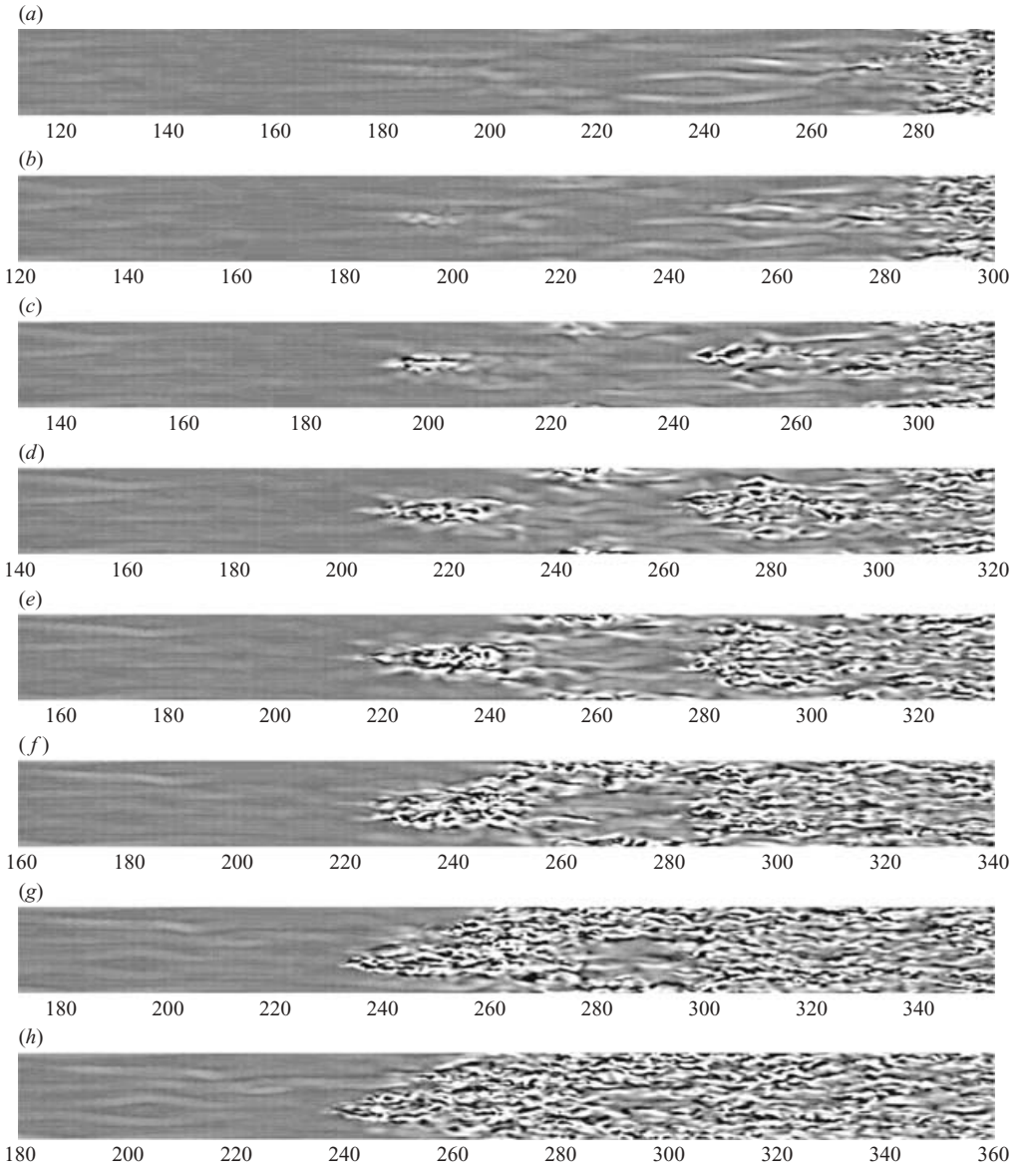

FIGURE 23. Instantaneous contours of wall-normal velocity fluctuation ($-0.005 \leqslant v \leqslant 0.005$) in ZPG. The plane is located at $y/\delta_0 = 0.11$. The frames correspond to the same instants in figure 22.

In the case of APG, a similar time sequence to figures 21 and 22 is recorded, and is shown in figures 27 and 28. Two spots are observed; one in the middle of the span, and the second immediately downstream at the periodic boundary. Both spots spread quickly, merge, and fill the entire span at a much faster rate than the ZPG simulation. The laminar, or quiet, region between the spots is therefore short-lived; it is completely absent from figure 28(*e*), of the sequence. This should be contrasted with figure 23 of the ZPG simulation, where the quiet region diminishes in size, but can still be identified in the last two snapshots of the time sequence. The faster spreading

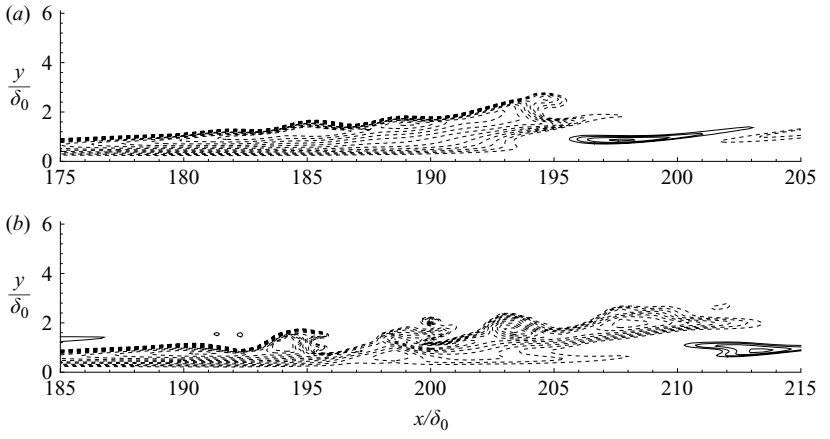

FIGURE 24. Instantaneous contours of streamwise velocity fluctuation ($-0.3 \leqslant u \leqslant 0.3$) in ZPG, at times corresponding to the instances in figure 21(a, b). The side view shown is a plane through the spot inception location. Dashed contours indicate negative values.

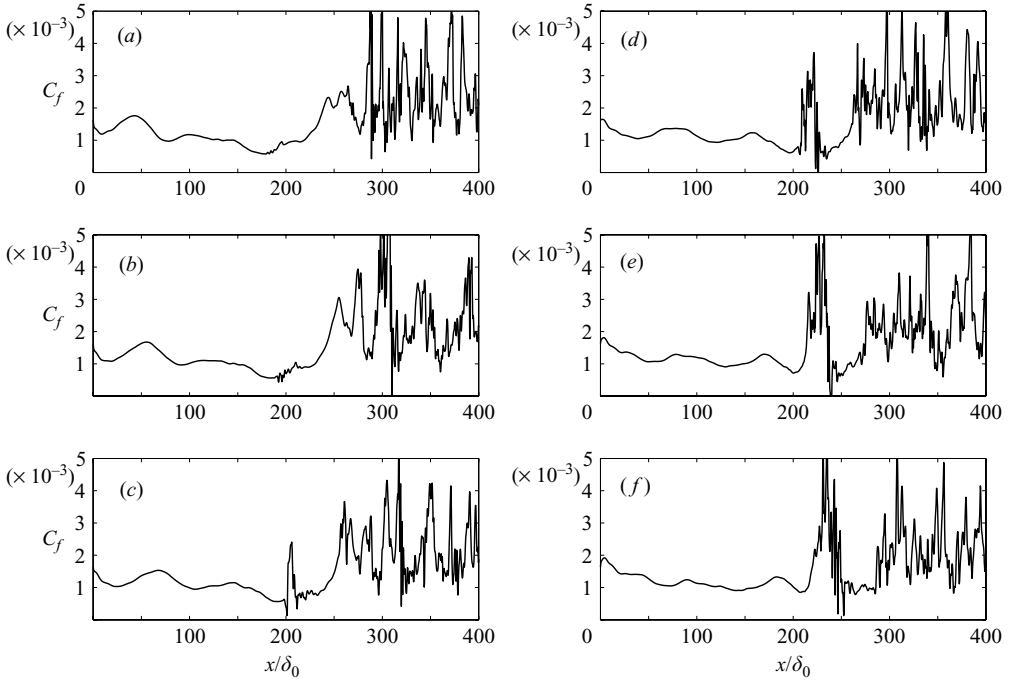

FIGURE 25. Instantaneous skin friction at different times. The times correspond to figure 21(a–f). The skin friction is calculated along a line bisecting the streak which hosts the spot formation.

in APG is in accord with the experimental literature (Gostelow *et al.* 1993; Seifert & Wygnanski 1995).

A side view of breakdown of a perturbation jet is shown in figure 29. The snapshots of streamwise velocity fluctuations correspond to the first three instances of figure 27.

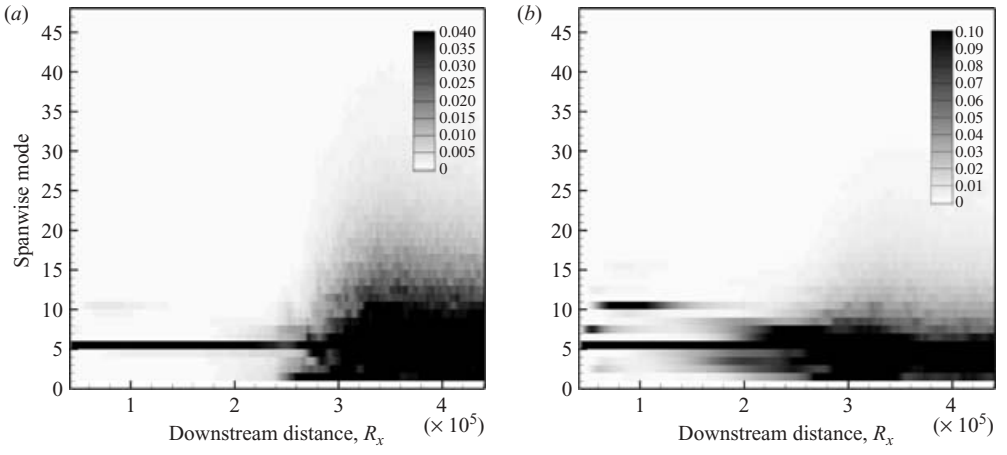

FIGURE 26. Energy content in the streamwise velocity fluctuations versus spanwise mode and Reynolds number. (*a*) $y/\delta = 0.1$; (*b*) $y/\delta = 2/3$.

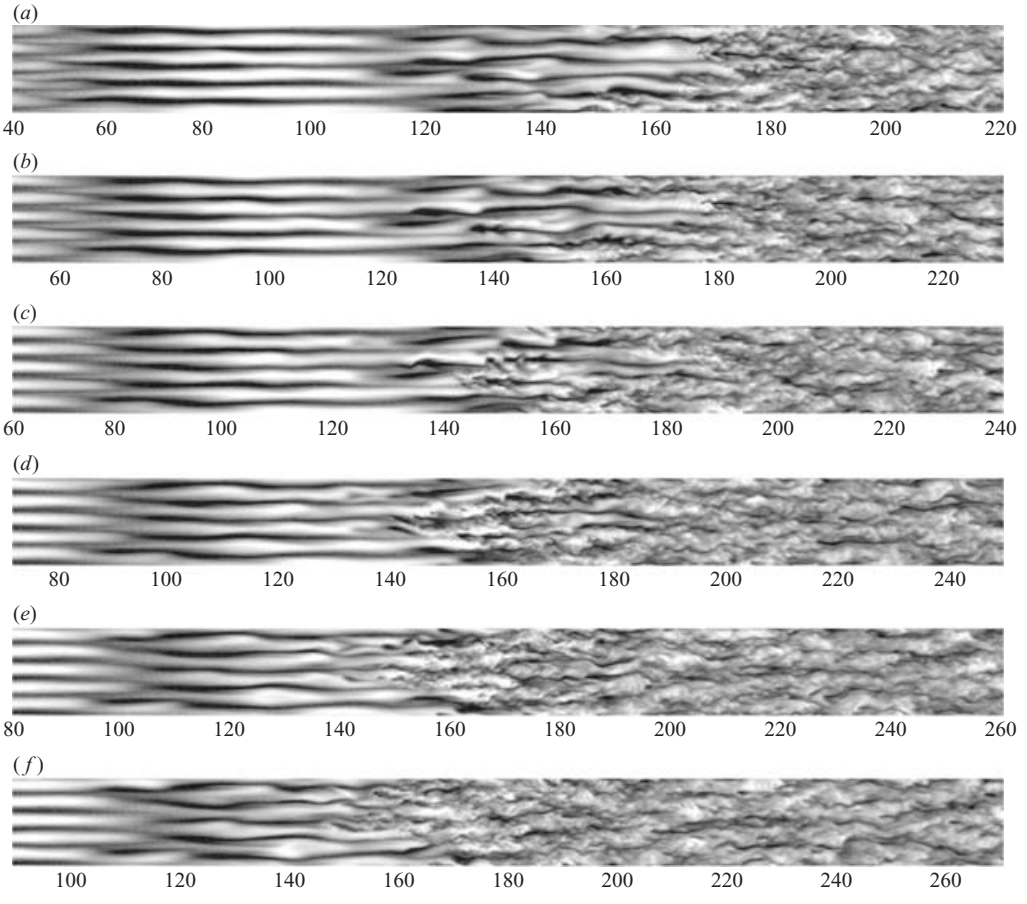

FIGURE 27. Instantaneous contours of streamwise velocity fluctuation ($-0.2 \leqslant u \leqslant 0.2$) in APG, $\beta = -0.14$. The plane is located at $y/\delta_0 = 0.75$, and the frames translate in the flow direction at half the free-stream velocity.

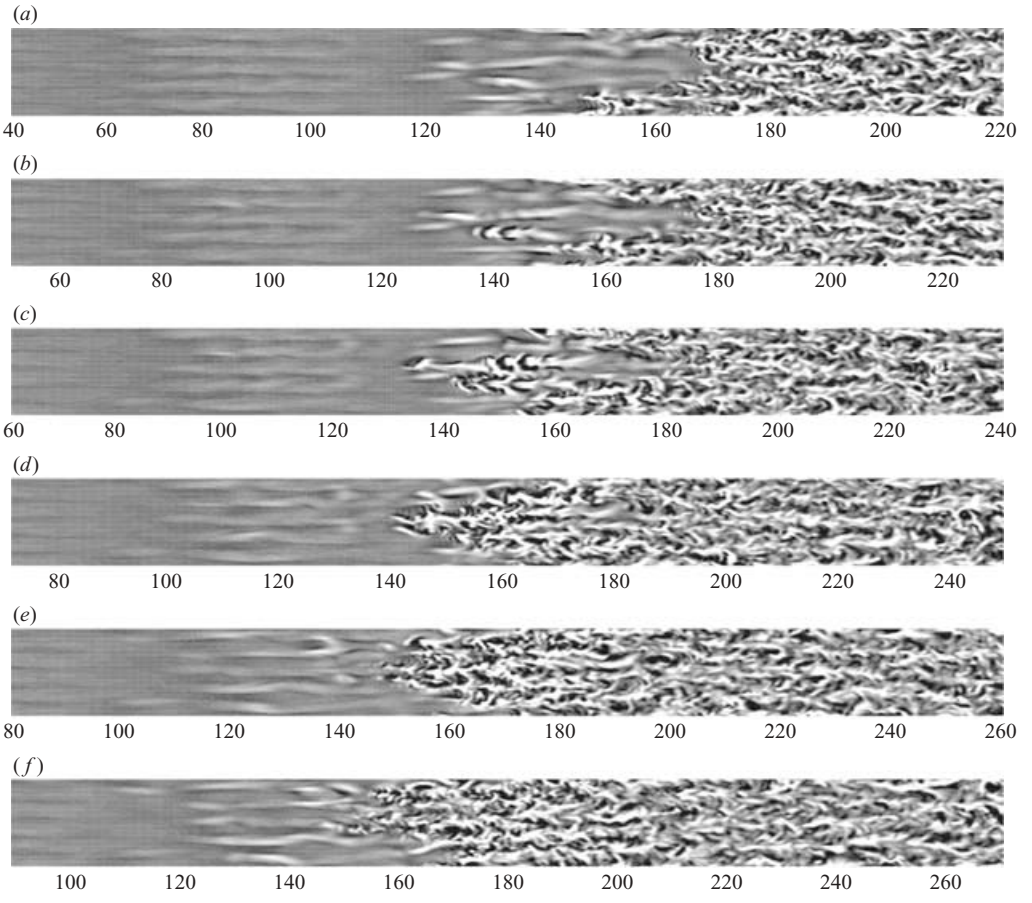

FIGURE 28. Instantaneous contours of wall-normal velocity fluctuation ($-0.05 \leqslant v \leqslant 0.05$) in APG, $\beta = -0.14$. The plane is located at $y/\delta_0 = 0.75$, and the frames correspond to the same time instants as in figure 27.

The instability, of inflection-point type, affecting the backward jets is captured well in the figure, and clearly starts near the free stream.

A sequence of instantaneous skin friction curves through the turbulent spot are shown in figure 30. The quiet region between the patch of turbulence and the downstream fully turbulent boundary layer is smaller than in ZPG. The spots spread quickly in APG and this quiet region disappears from the skin friction plots.

7. Conclusion

In orderly transition, the influence of pressure gradient on the stability of boundary layers is well established in the literature. In zero and favourable pressure gradients, Tollmien–Schlichting waves are subject to a weak viscous instability. In adverse conditions, the velocity profile becomes inviscidly unstable, and transition is much faster. However, in the presence of even moderate levels of free-stream turbulence, the natural route to transition is bypassed: Tollmien–Schlichting wave precursors are replaced by the interaction of continuous modes. Boundary-layer streaks become important. These disturbances, which are jets in the perturbation field, reach intensities

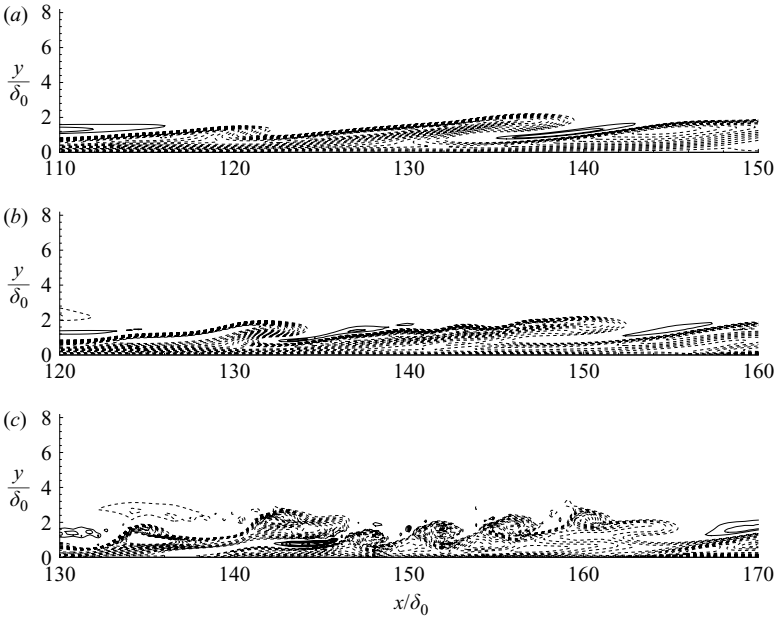

FIGURE 29. Instantaneous contours of streamwise velocity fluctuation ($-0.3 \leqslant u \leqslant 0.3$) in APG, at three times. The times coincide with first three frames of figures 27 and 28. The side view shown is a plane at mid-span, through the spot inception location. Dashed contours indicate negative values.

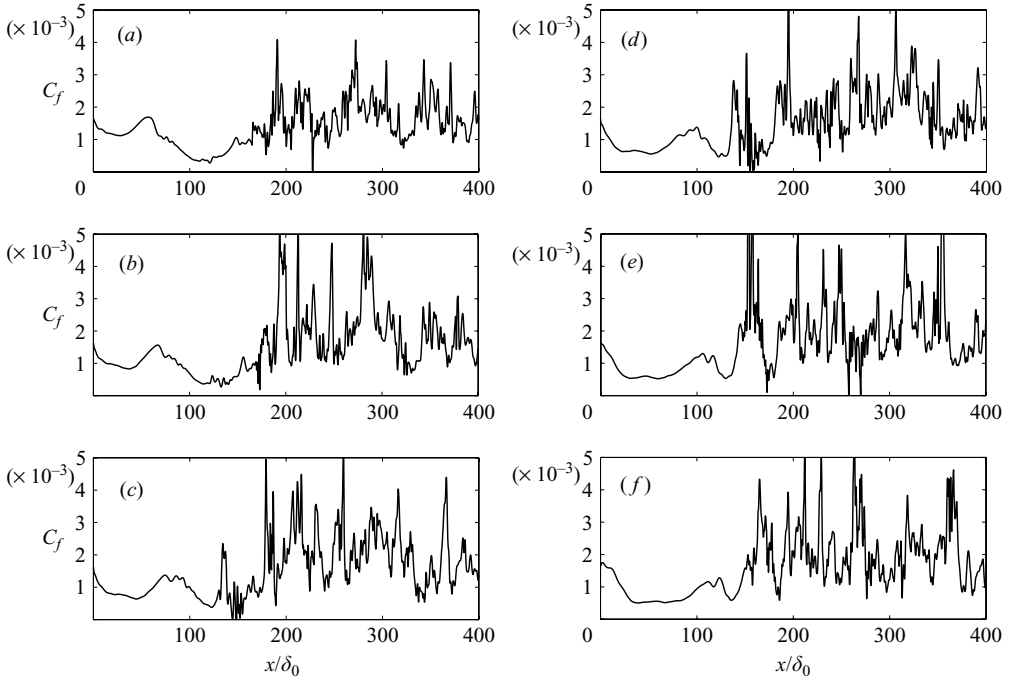

FIGURE 30. Instantaneous skin friction at different times. The times correspond to figure 27(a–f). The skin friction is calculated along a line bisecting the streak which hosts an instability leading to a turbulent spot.

of the order of 10 % of the free-stream velocity. The backward perturbation jets, induced by upward displacement of mean momentum, lift towards the edge of the boundary layer where they are exposed to the non-penetrating high-frequency forcing from the free stream. The streaks become unstable, and turbulent patches emerge (Jacobs & Durbin 2000).

The role of pressure gradient is no longer due to the Tollmien–Schlichting instability of the mean velocity profile. Instead, the influence of pressure gradient on the intensity of boundary-layer streaks, and consequently on transition, is studied. Linear theory (§ 4) and direct numerical simulations (§ 6) confirm that retarded flows generate stronger Klebanoff distortions than in ZPG. The correlation between streak intensity and transition location was verified using DNS of pairwise mode interactions which lead to transition. First, in ZPG, a fully turbulent boundary layer is realized earlier upstream when the low-frequency mode, and as a result the streaks, are of higher amplitude (figure 17). Pairwise mode interactions were also simulated in the presence of mean pressure gradient. Transition onset was upstream and the transition length shorter in APG (figure 19). The DNS results confirm the hypothesis that stronger perturbation jets, or streaks, are more unstable. This is consistent with the experimental observation that the bypass route to turbulence becomes independent of pressure gradient at high turbulent intensities (Abu-Ghannam & Shaw 1980). Under these conditions, the boundary-layer streaks are highly unstable, and adverse pressure gradient has little contribution; transition takes place swiftly, independent of the mean gradient in pressure.

This work is sponsored by the National Science Foundation and by the Department of Energy, under their ASC program at Stanford University. T. A. Z. acknowledges support by a Stanford Graduate Fellowship.

REFERENCES

Abu-Ghannam, B. J. & Shaw, R. 1980 Natural transition of boundary layers – the effects of turbulence, pressure gradient, and flow history. *J. Mech. Engng Sci.* **22**, 213–228.

Anthony, R., Jones, T. V. & LaGraff, J. E. 2005 High frequency surface heat flux imaging of bypass transition. *J. Turbomachinery* **127**, 241–421.

Benney, D. J. & Gustavsson, L. H. 1981 A new mechanism for linear and nonlinear hydrodynamic instability. *Stud. Appl. Maths* **64**, 185–209.

Bowles, R. G. & Smith, F. T. 1995 Short-scale effects on model boundary-layer spots. *J. Fluid Mech.* **295**, 395–407.

Brown, S. N. & Smith, F. T. 2002 On the variation of 'spot' properties with pressure gradient. *Eur. J. Mech.* B/*Fluids* **21**, 721–738.

Corke, T. C. & Gruber, S. 1996 Resonant growth of three-dimensional modes in Falkner–Skan boundary layers with adverse pressure gradients. *J. Fluid Mech.* **320**, 211–233.

Drazin, P. & Reid, W. H. 1995 *Hydrodynamic Stability*. Cambridge University Press.

Durbin, P. A. & Zaki, T. A. 2005 Continuous mode transition. *Transition and Turbulence Control*. Lecture Notes Series, Institute of Mathematical Sciences, National University of Singapore. World Scientific.

Goldstein, M. E. & Lee, S. S. 1992 Fully coupled resonant-triad interaction in an adverse-pressure-gradient boundary layer. *J. Fluid Mech.* **245**, 523–551.

Gostelow, J. P., Hong, G., Melwani, N. & Walker, G. J. 1993 Turbulent spot development under a moderate pressure gradient. *ASME Paper* 93-GT-377.

Gostelow, J. P., Blunden, A. R. & Walker, G. J. 1994 Effects of free-stream turbulence and adverse pressure gradients on boundary layer transition. *J. Turbomachinery* **116**, 392–404.

Grosch, C. E. & Salwen, H. 1978 The continuous spectrum of the Orr–Sommerfeld equation. Part 1. The spectrum and the eigenfunctions. *J. Fluid Mech.* **68**, 33–54.

Hodson, H. P. & Howell, R. J. 2005 Bladerow interactions, transition, and high-lift aerofoils in low-pressure turbines. *Annu. Rev. Fluid Mech.* **37**, 71–98.

Jacobs, R. G. & Durbin, P. A. 1998 Shear sheltering and the continuous spectrum of the Orr–Sommerfeld equation. *Phys. Fluids* **10**, 2006–2011.

Jacobs, R. G. & Durbin, P. A. 2000 Simulations of bypass transition. *J. Fluid Mech.* **428**, 185–212.

Kendall, J. M. 1985 Experimental study of disturbances produced in a pre-transitional laminar boundary layer by weak free stream turbulence. *AIAA Paper* 85-1695.

Kendall, J. M. 1991 Studies on laminar boundary layer receptivity to free stream turbulence near a leading edge. In *Boundary Layer Stability and Transition to Turbulence* (ed. X. Reda *et al.*). ASME-FED **114**, 23–30.

Kleiser, L. & Zang, T. A. 1991 Numerical simulation of transition in wall-bounded shear flows. *Annu. Rev. Fluid Mech.* **23**, 495–537.

Lasseigne, D. G., Joslin, R. D., Jackson, T. L. & Criminale, W. O. 1999 The transient period for boundary layer disturbances. *J. Fluid Mech.* **381**, 89–119.

Maslowe, S. A. & Spiteri, R. J. 2001 The continuous spectrum for a boundary layer in a streamwise pressure gradient. *Phys. Fluids* **13**, 1294–1299.

Morkovin, M. V. 1969 On the many faces of transition. *Viscous Drag Reduction* (ed. C. S. Wells). Plenum.

Nagarajan, S., Lele, S. & Ferziger, J. 2006 Leading edge effects in bypass transition. *J. Fluid Mech.* (in press).

Rosenfeld, M., Kwak, D. & Vinokur, M. 1991 A fractional step solution method for the unsteady incompressible Navier–Stokes equations in generalized coordinate systems. *J. Comput. Phys.* **94**, 102–137.

Seifert, A. & Wygnanski, I. J. 1995 On turbulent spots in a laminar boundary layer subjected to a self-similar adverse pressure gradient. *J. Fluid Mech.* **296**, 185–209.

Westin, K. J. A., Boiko, A. V., Klingmann, B. G. B., Kozlov, V. V. & Alfredsson, P. H. 1994 Experiments in a boundary layer subjected to freestream turbulence. Part I: boundary layer structure and receptivity. *J. Fluid Mech.* **281**, 193–218.

Wu, X. & Choudhari, M. 2003 Linear and nonlinear instabilities of a Blasius boundary layer perturbed by streamwise vortices. *J. Fluid Mech.* **483**, 225–248.

Wu, X. & Durbin, P. A. 2001 Existence of longitudinal vortices evolved from distorted wakes in a turbine passage. *J. Fluid Mech.* **446**, 199–228.

Wu, X., Jacobs, R. G., Hunt, J. C. R. & Durbin, P. A. 1999 Simulation of boundary layer transition induced by periodically passing wakes. *J. Fluid Mech.* **398**, 109–153.

Zaki, T. A. & Durbin, P. A. 2005 Mode interaction and the bypass route to transition. *J. Fluid Mech.* **531**, 85–111.